Deterministic reverberation from ocean ridges

Nicholas C. Makris, Lilimar Z. Avelino, and Richard Menis
Naval Research Laboratory, Washington, DC 20375

(Received 18 October 1994; accepted for publication 9 February 1995)

The deterministic relationship between low-frequency reverberation and detailed geomorphology is documented for wide-area insonifications of the western Mid-Atlantic Ridge. Charted reverberation registers precisely with extended ridges and has a high correlation with negative transmission loss, confirming previous analysis with lower resolution data [J. Acoust. Soc. Am. **95**, 1865–1881 (1993)]. For a given ridge, prominent returns come from steep escarpments and cliffs that face the bistatic source and receiving arrays. This was hypothesized in the above reference, but could not be proven without the higher resolution waveforms and more sophisticated charting procedures of the present analysis. Monostatic and bistatic returns from the same lineated ridge at $\frac{1}{2}$, $1\frac{1}{2}$, and $2\frac{1}{2}$ convergence-zone ranges are used to thoroughly document the registration with steep scarps. A decrease in resolution of the scattering site is also documented for increasing measurement range. Ambiguity from the horizontal receiving array is resolved by two independent methods that show close agreement for prominent returns. The first is an environmental symmetry breaking (ESB) technique that requires detailed knowledge of bathymetry to be incorporated into a range-dependent propagation model. The second is a global inversion of reverberation charts obtained from differing receiving-array locations and orientations. The global inversion requires no *a priori* environmental information and has not been previously applied to field data.

PACS numbers: 43.30.Gv, 43.30.Vh, 43.30.Pc

INTRODUCTION

Our objective is to document the deterministic relationship between prominent low-frequency reverberation and detailed ocean-basin geomorphology. The establishment of this relationship is significant because it provides a means of exploiting the only medium currently available for real-time remote sensing of wide areas of the ocean basin: low-frequency sound waves.

In the present analysis, we use acoustic waveforms transmitted from the vertical source array of a slowly moving research vessel (RV) to probe scattering sites spread over wide areas on the western flank of the Mid-Atlantic Ridge (MAR). Echo returns are measured with horizontally towed line arrays. Beamforming and range-dependent propagation modeling are used to chart the returns in a universal transverse mercator (UTM) coordinate system[1] to within roughly 100-m accuracy over hundreds of kilometers. The resulting reverberation charts are eventually coregistered with high-resolution bathymetry to identify mutually deterministic features.

Reverberation data were acquired in July 1993 during the Main Acoustics Experiment (MAE) of the Office of Naval Research Special Research Program (SRP).[2] Two research vessels were used to obtain mono- and bistatic reverberation from select bathymetric features of geomorphology characteristic to the MAR. Naturally occurring bottom morphology was exploited in the experimental design to minimize ambiguity in the receiving-array measurements and provide corridors for both direct-path [within $\frac{1}{2}$ convergence zone (CZ)] and longer range waterborne propagation to these select sites. Mono- and bistatic direct-path returns from one of these sites are compared with multiple CZ returns from the same site to thoroughly document the deterministic nature of the reverberation.

In a previous analysis[3] of MAR backscatter data measured during the Acoustic Reconnaissance Cruise (ARC) of 1991 it was shown that (1) prominent backscatter returns from extended ridges; (2) the most prominent returns follow waterborne propagation paths and therefore occur within the direct-path area and at $n+\frac{1}{2}$ CZ ranges; (3) spatial variations in measured backscatter are strongly dependent upon spatial variations in two-way transmission loss (TL). We confirm these results in the present analysis and prove a hypothesis made in Ref. 3. The hypothesis is that on a ridge that registers prominent reverberation, the strongest echoes return from scarps facing the source and receiving arrays. Because such scarps are typically less than 1 km wide (as will be shown in later sections), high-resolution waveforms are necessary to probe the geomorphology and test the hypothesis. The roughly 1.5-km range resolution of the earlier study was inadequate for this task. The roughly 47- to 375-m range resolution used in the present analysis is more than adequate. Such high-resolution imaging also requires a far more accurate charting procedure than the linear conversion between travel time and range that was adequate in Ref. 3. Therefore, we have developed a technique that accounts for refraction, bathymetric variation, multiple surface/bottom interaction, and the source beampattern via a range-dependent propagation model.[4]

In another improvement over previous work, ambiguity in the horizontal receiving array is resolved by two independent methods, rather than one. These methods show close agreement for prominent returns. The first is an environmen-

tal symmetry breaking (ESB) technique[3] that requires detailed knowledge of bathymetry for use in range-dependent propagation modeling. This was developed during analysis of ARC data primarily because the ARC track design was not conducive to more traditional ambiguity resolution methods that require redundant observations of the same features over varying receiving-array locations and orientations. The second method is a global inversion[5] (GI) of reverberation charts obtained over such varied observations. The MAE data set is ideal for the GI approach because the RV tracks were designed with ambiguity resolution as an essential theme. This inversion technique requires no *a priori* environmental information, has not been previously applied to field data, and has been shown to be superior to data stacking in simulations.[5] (We recommend Refs. 3 and 6 as background material and for relevant acoustic terminology, and Ref. 7 for relevant geological terminology.)

I. THE B′–C′ CORRIDOR EXPERIMENTS

The MAE actually consisted of a series of smaller experiments. These were designed around particular bathymetric features. Our analysis is exclusively geared toward what have become known as the B′–C′ Corridor Experiments, which comprised about 75% of the MAE. The B′–C′ corridor is the western portion of a much longer segment valley that extends to the MAR proper. The western end of the corridor is curtailed by a highly lineated outside-corner ridge roughly 30 km in length known as B′. The eastern end is sealed by a rounded inside-corner promontory known as C′. The essentially range-independent water-column sound-speed structure (shown in Fig. 1) coupled with the source depth (shown in Fig. 2) leads to a conjugate depth of 3800 m for the RV CORY CHOUEST transmissions, and a $\frac{1}{2}$ CZ range of roughly 33 km.

The B′–C′ corridor was selected for a variety of reasons.[8] First, it became clear that bathymetry to the west of the sites analyzed in Ref. 3 has greater excess depth and is therefore far more conducive to multiple CZ reverberation studies. Second, the B′–C′ corridor is roughly 2 CZ in length, and generally much deeper than the conjugate depth, except for B′ and C′ that protrude well above the conjugate depth contour at either end. This corridor morphology was a windfall for experimental design. As shown in Fig. 3, a source within the corridor 1/2 CZ from B′ is also $1\frac{1}{2}$ CZ from C′ and vice versa. Therefore direct-path returns can be simultaneously measured from B′ while $1\frac{1}{2}$ CZ returns are measured from C′, and vice versa. Furthermore, the ambiguous returns from along the corridor axis can be easily resolved at $\frac{1}{2}$ CZ range for either feature due to excess depth within the corridor, and at $1\frac{1}{2}$ CZ due to interaction with B′ or C′ at $\frac{1}{2}$ CZ. The situation is sketched with concentric circles of 1/2 and $1\frac{1}{2}$ CZ radius centered about two focal points of the track design. The mutual waterborne insonification of B′ and C′ from these focal points within the corridor is shown in Fig. 4 via parabolic-equation (PE) modeling.[9]

The bistatic tow-ship track design[8,10] is shown in Fig. 5. Star-shaped tracks are used to provide redundant measurements at differing array headings. The point of convergence

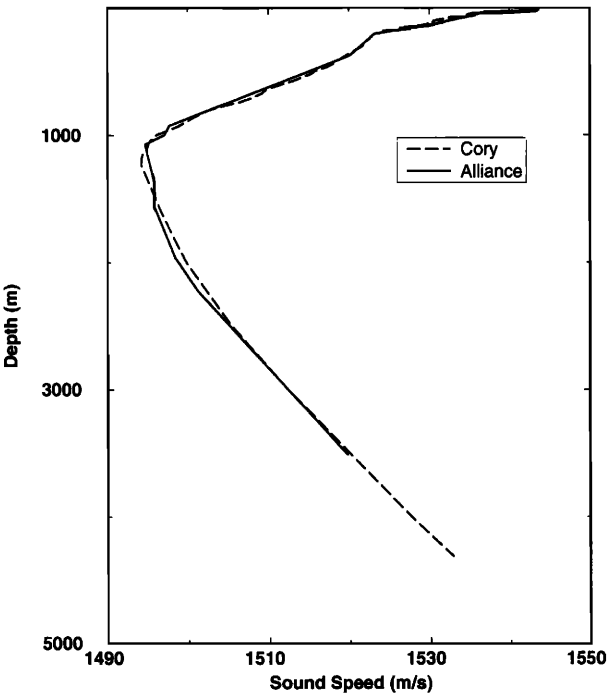

FIG. 1. Sound-speed profiles measured by the RV CORY CHOUEST via XBT on J201 20:02 Z at 26° 31′ N 47° 9′ W (near the Easternstar) and the RV ALLIANCE via CTD on J199 18:12 Z at 26° 34′ N 47° 59′ W (near the Westernstar). The close agreement between the profiles over significant spatial and temporal separations strongly supports the range/time-independent approximation used for the water-column sound-speed structure in this analysis. Archival data are used below 1830-m depth for the XBT.

of each star is placed at the eastern and western focal points. These tow-ship tracks are referred to as the Easternstar and Westernstar. Stars are more advantageous in the present environment than the traditional polygon patterns. This is because the analysis of Ref. 3 indicates that small variations in measurement position can lead to significant variations in reverberation due to bathymetry-induced variations in TL.

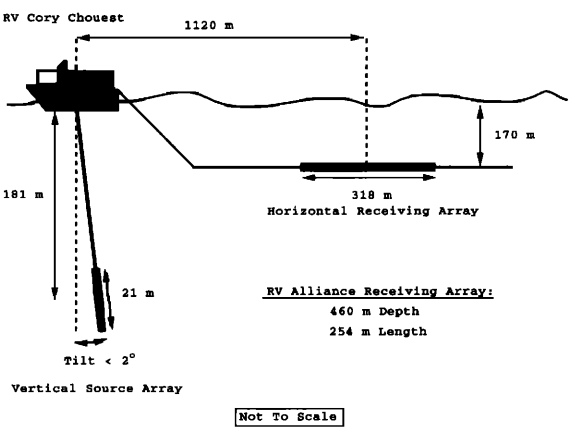

FIG. 2. A sketch of the RV CORY CHOUEST towing a vertical source array and horizontal receiving array. Array depths and orientation change with ship's speed. Conditions are shown for a typical tow speed of 3.5 kn. The spacing is 2.29 m for the ten-element source and 2.5 m for the 128-element receiver array. The RV ALLIANCE receiving array is at a mean depth of 460 m and has 128 elements at 2-m element spacing for this analysis. Only CORY CHOUEST and ALLIANCE receptions of CORY CHOUEST transmissions are analyzed in this paper.

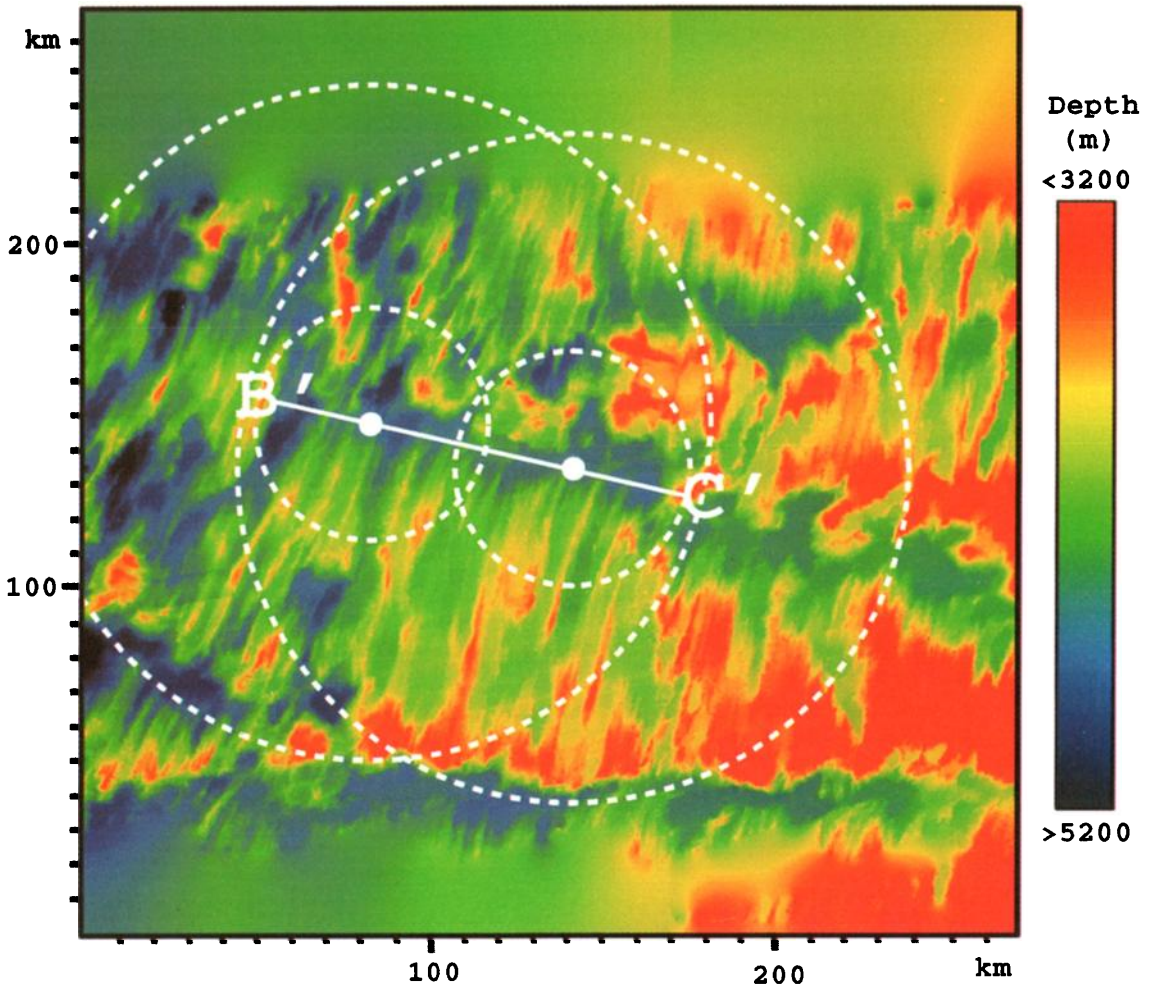

FIG. 3. Hydrosweep bathymetry from the SRP geophysical survey of 1992 sampled at 200-m intervals. Conjugate depth occurs at roughly 3800 m for the RV CORY CHOUEST source. The inside-corner ridge B′ and the outside-corner ridge C′ are bottom limited at either end of the B′–C′ corridor, which is a segment valley of positive excess depth. White dots at two focal points divide the roughly 2 convergence zone (CZ) corridor into thirds. Concentric circles of $\frac{1}{2}$ and $1\frac{1}{2}$ CZ radius from these focal points show how B′ and C′ can be simultaneously insonified from either foci. The circles also indicate other direct-path (within $\frac{1}{2}$ CZ) and $1\frac{1}{2}$ CZ areas where waterborne returns are expected to dominate backscatter. The tow-ship observations of Ref. 3 were made at roughly the easternmost intersection of the eastern $1\frac{1}{2}$ CZ circle with the northern cliffs of the segment valley.

Stars avoid the problem of comparing measurements with significantly different TL because they have a point of global convergence over all array headings. This is not the case with polygons. The RV CORY CHOUEST followed the central star patterns while the RV ALLIANCE surveyed the wings at $\frac{1}{2}$ CZ range about B′ and C′. The generally north–south orientation of the star legs is designed to: (1) keep endfire beams out of the corridor, (2) exploit the greater longitudinal extent of the 200-m resolution Hydrosweep bathymetry[11] for higher resolution beams near and at broadside, and (3) keep the ships in each other's lowest resolution endfire beams while surveying each site at $\frac{1}{2}$ CZ.

The CORY and ALLIANCE begin their tracks at close proximity, 0° bistatic separation, proceed to greater than 90° bistatic separation with respect to B′/C′ at $\frac{1}{2}$ CZ, and return to close proximity along a different path to help eliminate ambiguity. At their greatest separation of up to 1 CZ, single bottom-bounce forward scattering is available between the two ships. The hourglass patterns for the CORY and ALLIANCE provide $2\frac{1}{2}$ CZ returns from B′ and C′, respectively. The crisscross down the B′–C′ corridor gives a more general survey of the overall area. (For further information about the B′–C′ track design, as well as information about other experiments in the vicinity of B′ and C′, see Ref. 12.)

It is also fortunate that the two primary geological categories of ridges in the western MAR are spanned by B′ (an outside corner) and C′ (an inside corner).[7] Fine-scale geological data, including bathymetry at 5-m sampling, were collected over approximately rectangular areas (5×10 km) at central sites on B′ and C′ during the SRP Fine-Scale Geophysical Survey of May–June 1993. These data are to be compared with low-frequency reverberation measured during the B′–C′ Corridor Experiments to elucidate the scattering processes that cause reverberation from ocean ridges. For example, a preliminary comparison is given in Sec. VI. Vertical bottom-mounted arrays were also deployed within these fine-scale sites at B′ and C′ to obtain information on the vertical directionality of reverberation in the proximity of the scarps.[13]

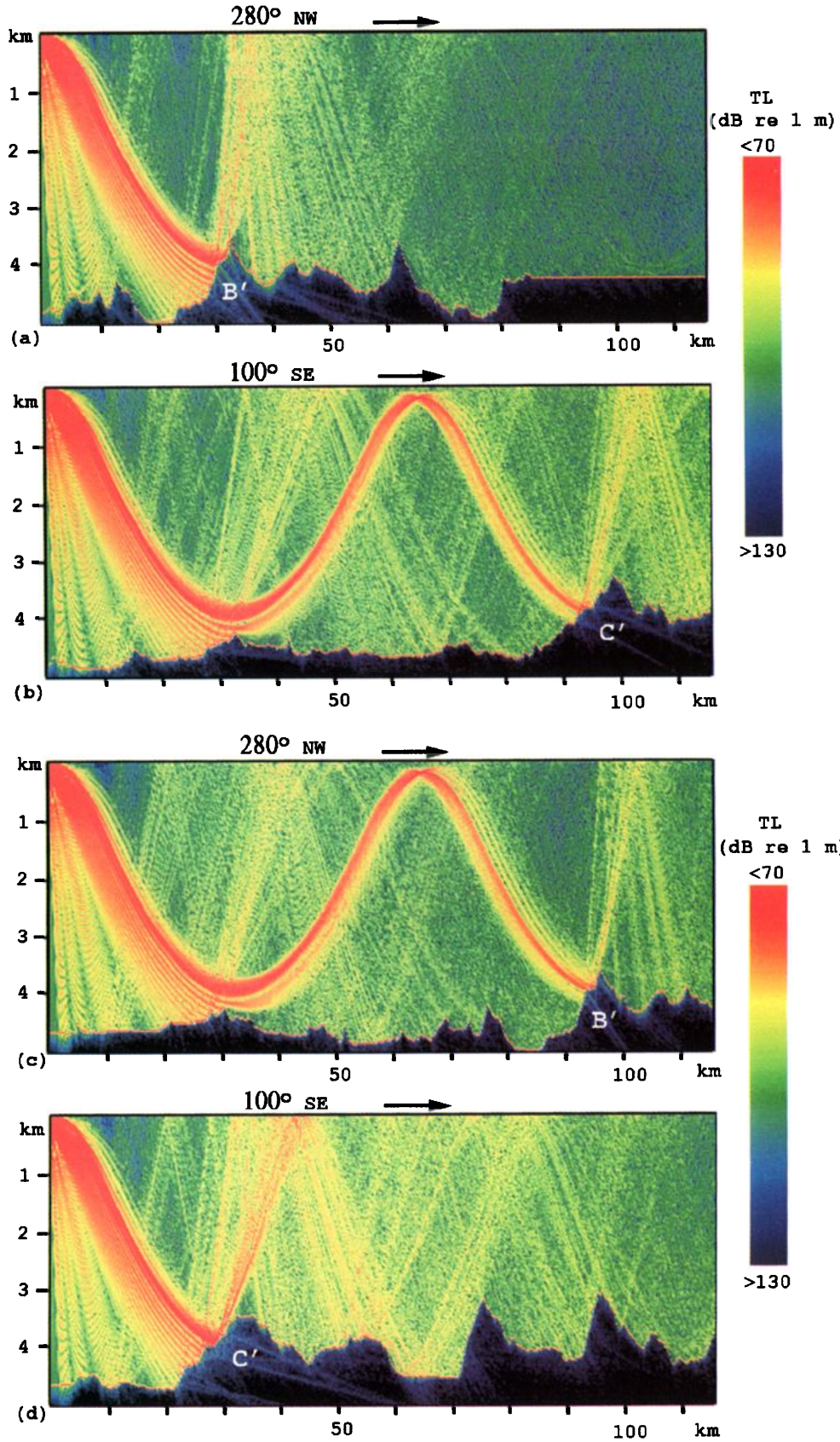

FIG. 4. Transmission loss (TL) for range-depth cross sections of the ocean showing insonification of B′ and C′ from the two focal points in the B′–C′ corridor of Fig. 3. As noted in Ref. 3, backfacing scarps are generally the most intensely insonified. Evident are three sidelobes of the ten element array that provide short-range insonification within the direct-path area. Refraction of the main beam is evident at the outskirts of the direct-path area and beyond, as are Lloyd mirror interference fringes due to the source's proximity to the pressure release surface. The TL is computed using the PE for ten cw sources at $f=268$ Hz corresponding to the actual projectors in the array. The source array is steered to broadside, or zero depression, for all measurements in this paper. A Westernstar-center source insonifies B′ in (a) and C′ in (b). An Easternstar-center source insonifies B′ in (c) and C′ in (d).

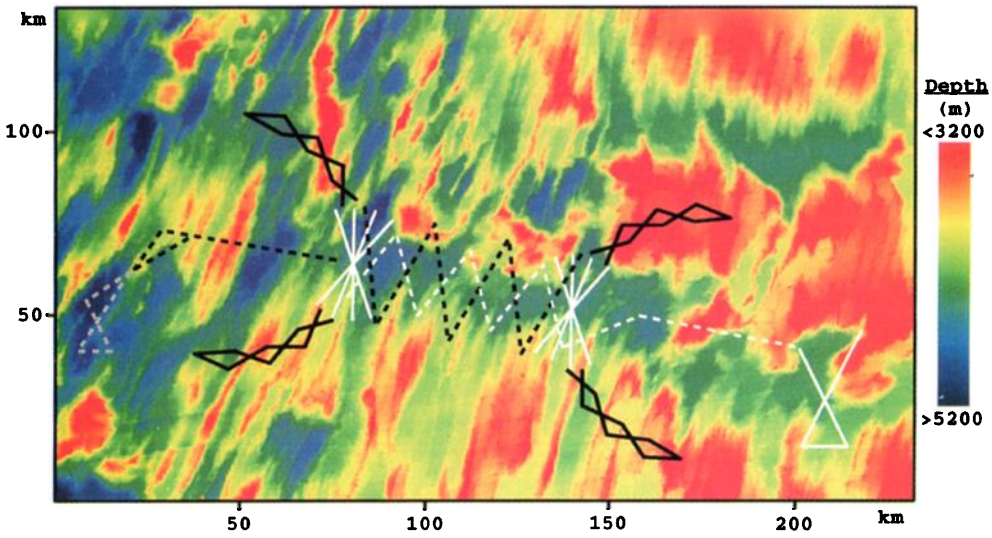

FIG. 5. The bistatic tow-ship tracks for the RV CORY CHOUEST (white lines) and RV ALLIANCE (black lines) overlain on bathymetry describe the geometry of the B′–C′ corridor experiments. The CORY star-shaped tracks within the corridor and the ALLIANCE tracks forming wings about B′ and C′ economically provide $\frac{1}{2}$ and $1\frac{1}{2}$ CZ waterborne reverberation from B′ and C′ over a wide range of bistatic angles. The easternmost CORY hourglass tracks provide $2\frac{1}{2}$ CZ waterborne backscatter from B′. The westernmost ALLIANCE hourglass tracks (in grey) provide $2\frac{1}{2}$ CZ backscatter from C′. Dotted lines indicate tracks not directly relevant to this analysis. The southern ALLIANCE tracks forming wings about B′ and C′ were slightly modified at sea from the geometry shown.

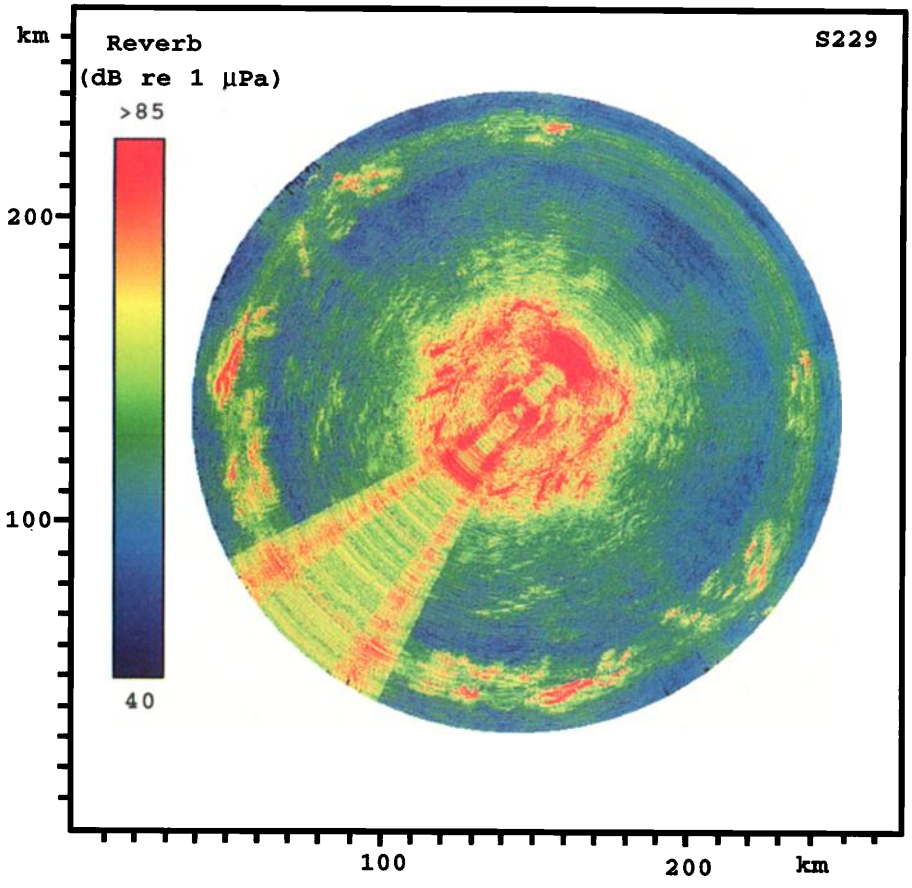

FIG. 6. A reverberation chart for the τ=0.5 s duration, f=268 Hz center frequency, cw transmission s229 over the area shown in Fig. 3. The RV CORY CHOUEST source/receiver is within 1 km of the Easternstar center. All returns are mirrored about the array axis (224°) due to right–left ambiguity. Prominent returns occur within the direct-path area and at $1\frac{1}{2}$ CZ range. The 375-m range resolution of these returns provides a detailed image of the geomorphology including the B′ ($1\frac{1}{2}$ CZ range) and C′ ($\frac{1}{2}$ CZ range) features at locations corresponding to those in Fig. 3. Travel time to range conversion is done by a range-dependent propagation model that includes the effects of refraction, multiple surface/bottom interaction, and source beampattern. Poor resolution due to endfire occurs within ±24° of the array axis, where tow-ship noise is evident in the forward sector. The mean reverberation level is 60.9 dB *re*: 1 μPa, the median is 59.6 dB *re*: 1 μPa, and the standard deviation is 8.5 dB. The sample probability (or histogram) for this reverberation chart has a 0.96 correlation coefficient with a Gaussian distribution of the same mean and variance.

II. WIDE-AREA REVERBERATION CHARTS FROM THE B′–C′ CORRIDOR

In this section, reverberation charts are presented for monostatic measurements made near the center of the Easternstar and Westernstar, respectively. These measurements survey the seafloor over wide areas from directly below the tow ship (RV CORY CHOUEST) to ranges beyond $1\frac{1}{2}$ CZ. By analysis of these charts, we demonstrate the success of the experimental design in providing (1) prominent returns from both B′ and C′ in a given measurement, (2) prominent returns from many other bottom features of distinct geomorphology and geoacoustic composition, and (3) redundant observations of the same bottom features with sufficiently varied receiver-array orientations for ambiguity resolution. The deterministic relationship between prominent returns and backfacing scarps is also shown via precise registration between reverberation and directional derivative (DD) of the bathymetry. Due to recent advances in data acquisition and processing, it was possible to obtain these results at sea within hours of the measurements[12] but with a less precise charting procedure.

In this paper, only RV CORY CHOUEST transmissions are examined because of the significantly greater strength and directionality of the Cory's source array compared to that of the RV ALLIANCE. Additionally, the Cory's source array is steered to 0° depression angle (i.e., horizontally) for all transmissions to be analyzed in this paper. In Secs. II–V, all wide-area reverberation, TL, and scattering strength charts are plotted over the same area as the bathymetry in Fig. 3. Bistatic charts for ALLIANCE reception of CORY transmissions are given in Sec. VI, where both mono- and bistatic reverberation is compared with Hydrosweep and fine-scale bathymetry of B′.

A. Charting and navigation

Wide-area reverberation charts from the B′–C′ corridor are generated in the same manner as in Ref. 3 except that a range-dependent ray trace is used to determine the relationship between the travel time and range of scattering sites rather than a linear conversion. The ray trace includes the effects of refraction, multiple surface/bottom interaction, and bathymetry. The errors associated with not including these effects can be far greater than the 47- to 375-m range resolution of this study. These errors are most severe (>1 km) at sites where multiple surface/bottom interacting paths produce the dominant reverberation, such as in the shadow region between $\frac{1}{2}$ and $1\frac{1}{2}$ CZ. Similarly, not including refraction in charting returns from the outskirts of the direct-path area and at $1\frac{1}{2}$ CZ can lead to errors on the order of 500 m in range. This will be discussed in detail in a future article.[4]

A total of 1440 range-depth ray trace radials spanning the full 360° azimuth are computed for each wide-area chart. These sample the environment at 0.25°, or roughly one-quarter of the nominal broadside resolution of the receiving array. Global positioning system (GPS) navigation is used to locate the RVs to within 100 m in decimal degrees.[14] (Higher-resolution satellite navigation is available but unnecessary for the present analysis.) Conversion between decimal degrees and UTM are made via a United States Geological Survey (USGS) geodetic reference system that is accurate to within roughly 1 m.[15] Therefore, the primary sources of charting error are in the conversion from travel time to range and in the ship's positioning, which are both generally less than 100 m.

B. Variance of the imaging system

The standard deviation of a pixel value in a reverberation chart is now estimated. For simplicity, it is assumed that the active transmission is not affected by propagation-induced scintillation during the forward and return trip from a seafloor scattering site. Clearly, this assumption is best suited for waterborne paths, and is based upon the great temporal/spatial stability found in the water-column sound-speed structure discussed in the previous section. The transmitted waveform's interaction with the seafloor scattering area is assumed to completely randomize the return such that the real and imaginary temporal components of the instantaneous scattered field are identically distributed and uncorrelated zero-mean Gaussian random variables.[16] The instantaneous intensity of the return is then exponentially distributed, and the time-averaged intensity is gamma distributed[16,17] with degrees of freedom μ corresponding to the time-bandwidth product TB of the scattered field. The time-bandwidth product is an approximate measure of the number of independent and instantaneous intensity fluctuations averaged together over the measurement time T. The bandwidths for constant wave (cw) and linear frequency modulated (LFM) transmissions analyzed in this paper are $B=2$ and 55 Hz, respectively. The averaging time for cw transmissions analyzed in this paper is $T=0.25$ s, leading to the degrees of freedom $\mu=1$, corresponding to a peak amplitude measurement ($\mu-1$ must be positive semidefinite). The averaging time for LFM transmissions is $T=0.0625$ s for RV CORY CHOUEST receptions and $T=0.0553$ s for RV ALLIANCE receptions analyzed in this paper, leading to respective degrees of freedom $\mu=3.4$ and 3.0, respectively. (We ignore averaging of overlapping beams because the measurements are not independent.) If the reverberation level in dB *re*: 1 μPa for a given pixel in a reverberation chart is $R=10\log$ (mean-square pressure), the standard deviation of the reverberation level R is

$$\sigma=4.34\sqrt{\zeta(2,\mu)}, \tag{1a}$$

where

$$\zeta(v,\mu)=\sum_{k=0}^{\infty}\frac{1}{(\mu+k)^v}, \quad \text{for } v>1, \quad \mu\neq 0,-1,-2,-3,\ldots, \tag{1b}$$

is Riemann's zeta function where $\zeta(2,1)=\pi^2/6$. The standard deviation given in Eq. (1) is solely a function of the degrees of freedom μ, and can be deduced from expressions derived in Ref. 18 for the standard deviation attributed to the noise of "multiple distant sources," from which the degrees of freedom of independent intensity samples are supposed to arise in that application. However, the relevant derivation in terms of the time-bandwidth product of a fluctuating field is given in Ref. 19. With degrees of freedom μ for the cw reverberation charts, the standard deviation at a given pixel is roughly

5.6 dB, while for the LFM reverberation charts the standard deviation at a given pixel is roughly 2.5 dB. These standard deviations comprise a small fraction of the range of values spanned in the reverberation charts to be presented. For example, prominent returns that register with well-defined geomorphology typically stand above the background reverberation by tens of decibels (many standard deviations) and therefore are considered to be deterministic.

The most statistically significant information about seafloor characteristics is found at sites insonified by waterborne paths. This is because returns from these sites have intensities that are much larger than ambient noise or clutter from other multiple surface/bottom interacting returns arriving in the same beam and time window. Returns from shadow zones are least statistically significant because they are often of the same level as noise or clutter. Additionally, a strong return often comes from the same range but a different azimuth as a weak return when the main beam interacts with the bottom for one azimuth but not another. In this case, the strong return can corrupt the measurement of the weaker return via sidelobe leakage in the beamformer. For example, the sidelobe level of the beamformed output of the receiving array is typically 30–35 dB down from the main lobe for arbitrary steering directions and cw measurements,[20] while prominent returns often stand above background reverberation from adjacent ranges by greater than 30 dB.

In the present analysis, each instantaneous reverberation fluctuation measured by the towed-array imaging system contains averaged or blurred information about a wide spatial area of the seafloor. Even for ranges as close as $\frac{1}{2}$ CZ, the cross-range resolution of the receiving array at broadside is typically 500 m, while the range resolution varies with the bandwidth of the transmission from tens to hundreds of meters for an instantaneous measurement ($\mu=1$). Significant environmental variations occur over these scales, relative to the roughly 5- to 6-m acoustic wavelength of the present study. Therefore, only the mean scattered intensity of an aggregate of scatterers can be determined by the towed-array imaging system, even for an instantaneous measurement where resolution is optimal. (However, instantaneous measurements have the highest variance, as noted in the preceding paragraphs. While temporal averaging reduces the variance, it also reduces the range resolution. A compromise between these conflicting interests is adopted and discussed further in Sec. VI where high-resolution LFM transmissions are analyzed.)

C. Easternstar

We follow the convention of Ref. 21 and identify different transmissions by what is referred to as their segment number. A segment is a period (typically 12 min) during which a series of distinct cw and/or LFM waveforms were transmitted during the MAE. The exact time of a given transmission, and of a given segment, can be found from tables in Ref. 21, where detailed information about the waveform design is also given. The location of the RVs can be determined from these tables because the segment number, center frequency, and duration of a cw transmission identify the transmission time.

The reverberation chart shown in Fig. 6 is for a $\tau=0.5$ s duration cw transmission at center frequency $f=268$ Hz transmitted during segment s229. The range resolution is $\Delta r = c\tau/2 = 375$ m for a nominal sound speed $c=1500$ m/s. This cw signal was transmitted 0.8 km east and 0.6 km north of the Easternstar center (26° 26.825′ N 47° 9.375′ W). The general characteristics of the reverberation are similar to those in Fig. 7 of Ref. 3 except the range resolution is increased by a factor of 8 and the cross-range resolution is increased by a factor of 2. High-level reverberation is found throughout the direct-path area and in a series of discrete returns at $1\frac{1}{2}$ CZ range. Symmetry about the 224° heading (clockwise from true north) of the tow ship is due to right–left ambiguity of the receiving array. The elevated level appearing in the sector about forward endfire is due to tow-ship noise. The generally elevated level of reverberation in a diffuse ring about $1\frac{1}{2}$ CZ range is due to strong returns from other azimuths leaking in through sidelobes of the receiving array that were roughly 30–35 dB below the mainlobe.[20] Cross-range resolution is equal to $r\beta(\theta)$, where r is the range from the receiving-array center, and the resolution of the receiving array $\beta(\theta)$ over azimuth θ is given in Ref. 3. Because a Hamming window is used, the nominal broadside resolution is $\beta(\pi/2)\approx 1.3°$, and the endfire resolution is $\beta(0) = \beta(\pi)\approx 24.3°$. (A derivation of the azimuthal resolution of a line array appears in Ref. 22. The relevance of β to charting reverberation is discussed in Ref. 5.) Because the locations of the true returns are invariant to receiving array orientation, ambiguity in prominent returns can be sorted qualitatively by visual comparison with the reverberation chart of another nearby measurement. For this purpose, a reverberation chart for cw transmission s918 is shown in Fig. 7(a). It has the same pulse duration and center frequency as segment s229 but was transmitted 0.2 km west and 1.8 km south of the Easternstar center with a receiving array orientation of 179°.

Once ambiguity has been resolved by this visual method, a relationship between prominent returns and bathymetry is evident by comparison with Fig. 3. A more accurate comparison is made by overlaying charted reverberation on the directional derivative (DD) of bathymetry. The DD is defined in Ref. 3 as the dot product of the gradient of bathymetry with the horizontal unit vector pointing in the direction of the source or receiver location. For a monostatic geometry, the DD gives a measure of the bottom slopes facing the tow-ship observation position. By registration of prominent reverberation with the DD in Fig. 7(b) and (c), it is evident that the morphology of acoustic returns closely matches the morphology of the local ridge structure in regions where waterborne paths are available, such as the direct-path area and at $1\frac{1}{2}$ CZ ranges. Prominent returns are primarily charted to backfacing scarps, except at endfire where resolution is insufficient to resolve the scarps. Because prominent returns so thoroughly cover backfacing scarps, a DD chart without overlain reverberation is shown in Fig. 7(d) for comparison. The reverberation charted to the C′ feature within the direct-path area and the B′ feature at $1\frac{1}{2}$ CZ range provides valuable examples of the relationship between prominent returns and backfacing scarps. A higher threshold is used to plot prominent returns at $1\frac{1}{2}$ CZ in Fig.

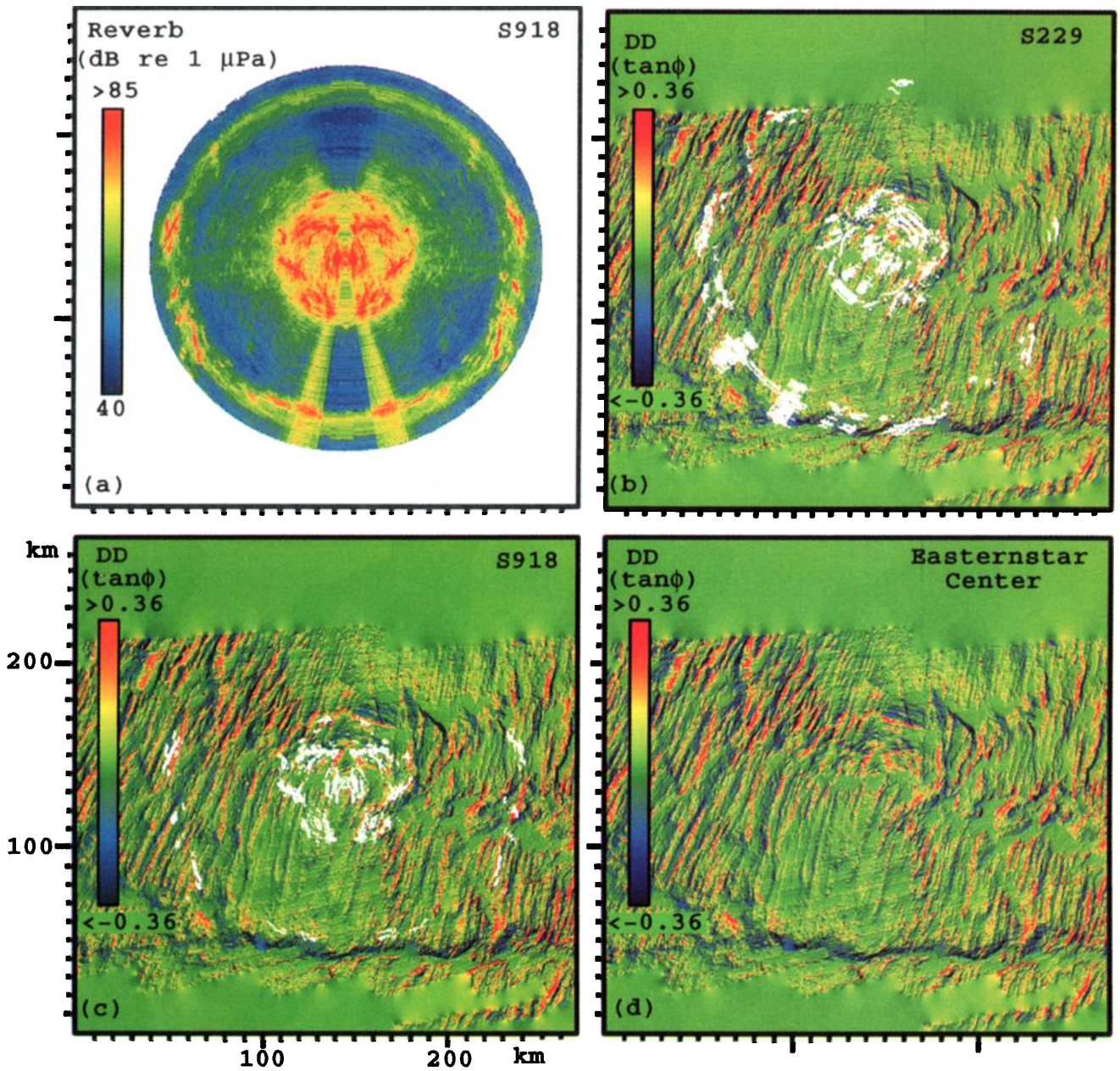

FIG. 7. (a) Same as Fig. 6 except for cw transmission s918 at receiver array heading 179°. The mean reverberation level is 60.1 dB *re*: 1 μPa, the median is 58.8 dB *re*: 1 μPa, and the standard deviation is 8.5 dB. Right–left ambiguity can be qualitatively resolved by comparing prominent returns with those in Fig. 6(b). Prominent reverberation from cw transmission s229 (see Fig. 6 for details) is overlain in white on the color directional derivative (DD) of bathymetry with respect to the Easternstar center which is approximately the monostatic source/receiver location. The DD is the inner product of the gradient of bathymetry with the horizontal unit normal pointing in the direction of the observation position. The DD is given by tan φ, where φ is the slope angle of the bathymetry in the direction of the observation. Only direct-path area returns above 82 dB *re*: 1 μPa and $1\frac{1}{2}$ CZ returns above 75 dB *re*: 1 μPa are overlain. (c) Same as (b) except for cw transmission s918 and only direct-path area returns above 82 dB *re*:1 μPa and $1\frac{1}{2}$ CZ returns above 82 dB *re*: 1 μPa are overlain. (d) Directional derivative with respect to the Easternstar center without overlain reverberation. Comparison of (b) and (c) enables qualitative ambiguity resolution. Comparison with (d) gives a qualitative indication that prominent reverberation returns from scarps facing the source/receiver array. Red indicates positive DD (facing the source/receiver array) and blue indicates negative DD (facing away from the source/receiver array).

7(c) than in Fig. 7(b). This shows that choice of the threshold leads to a trade-off between near perfect registration with backfacing scarps for the most prominent returns as in Fig. 7(c), and a broader area of prominent returns with registration that is less perfect but still high as in Fig. 7(b).

Comparison of prominent returns charted to $1\frac{1}{2}$ CZ ranges for segments s229 (in Fig. 6) and s918 [in Fig. 7(a)] indicates that changes in measurement position on the order of 1 km can lead to significant variations in reverberation from a given backfacing scarp. Because these variations are typically over many pixels and are much greater than the 5.6-dB standard deviation, we believe that they are deterministic and due to bathymetry-related changes in TL. Specifically, the deeper penetrating portion of the source's main beam is often deterministically cut off by bathymetry at $\frac{1}{2}$ CZ. The depth of the cutoff is variable as is apparent in Figs.

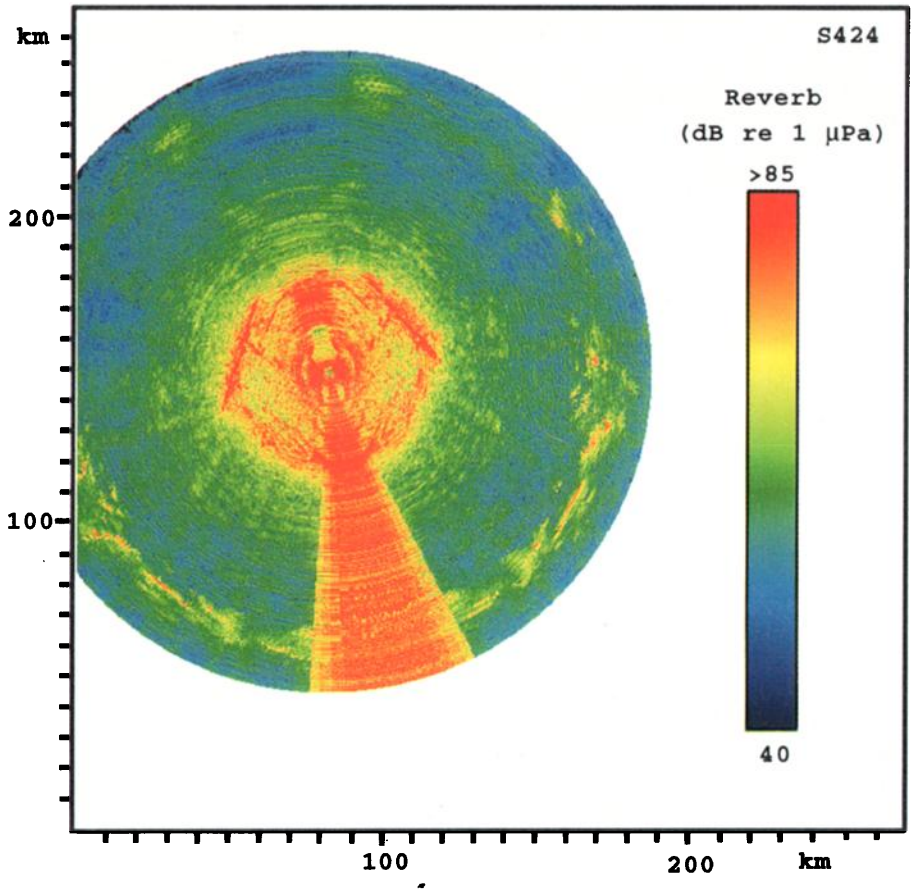

FIG. 8. Same as Fig. 6 except for cw transmission s424 measured within roughly 1 km of the Westernstar center at receiver array heading 168°. B′ is now evident at $\frac{1}{2}$ CZ and C′ at $1\frac{1}{2}$ CZ range. The mean reverberation level is 61.8 dB *re*: 1 μPa, the median is 59.5 dB *re*: 1 μPa, and the standard deviation is 8.9 dB. The sample probability (histogram) for this reverberation chart has a 0.88 correlation coefficient with a Gaussian distribution of the same mean and variance.

4 and 18. Therefore slight variations in source position can lead to corridors where deeper penetrating main-beam insonification is possible at $1\frac{1}{2}$ CZ. This was realized at sea, and minor modifications to the ship tracks were often employed to accommodate the bathymetry.

D. Westernstar

By similar analysis of measurements made near the center of the Westernstar (26° 32.898′ N 47° 46.452′ W), prominent returns are unambiguously charted to the B′ feature within the direct-path area and to the C′ feature at $1\frac{1}{2}$ CZ. This is evident by inspection of reverberation charts for the s424 and s522 cw measurements (of the same pulse duration and center frequency as segment s229) shown in Figs. 8 and 9(a), respectively. Specifically, the s424 cw signal was transmitted 0.4 km west and 0.8 km north of the Westernstar with an array heading of 168°, and the s522 cw signal was transmitted 0 km west and 0.2 km north of the Westernstar with an array heading of 206°. By inspection of Fig. 9(b)–(d) it is apparent that prominent returns are again primarily charted to backfacing scarps, except at endfire where resolution is insufficient. At the B′ feature in particular, a series of steep scarps running nearly the full length of the roughly 30-km-long ridge provide strong returns. The level of returns from a given scarp on B′ is strongly dependent upon azimuthal variations in the incident and scattered angle, as will be shown in Sec. VI.

III. CORRELATING MEASURED REVERBERATION WITH MODELED BLURRED TWO-WAY TRANSMISSION LOSS

We follow the methodology previously developed in analysis of ARC data,[3] and compute the two-way TL to scattering sites on the seafloor and back to the receiving array using the PE. We do so for 360 range-depth radials at 1-deg azimuthal spacing about the respective star center, using the high-resolution Hydrosweep bathymetry sampled at 200-m intervals and the sediment parameters of Ref. 3. A ten-element source array is used to compute forward transmission loss TL_f to respective scattering sites and a reciprocal point source is used to compute back transmission loss TL_b from the scattering sites to the receiving array. All modeling is for a cw signal at $f=268$ Hz. (For example, range-depth cross sections of TL_f appear in Figs. 4 and 18.)

The area of each scattering site is incorporated by convolving the antilog of the two-way transmission loss (TL_f+TL_b) with the spatially varying resolution of the receiving array $A=r(\Delta r)\beta$, where β and r are defined in Sec. II, and Δr is the range resolution of the measurement which

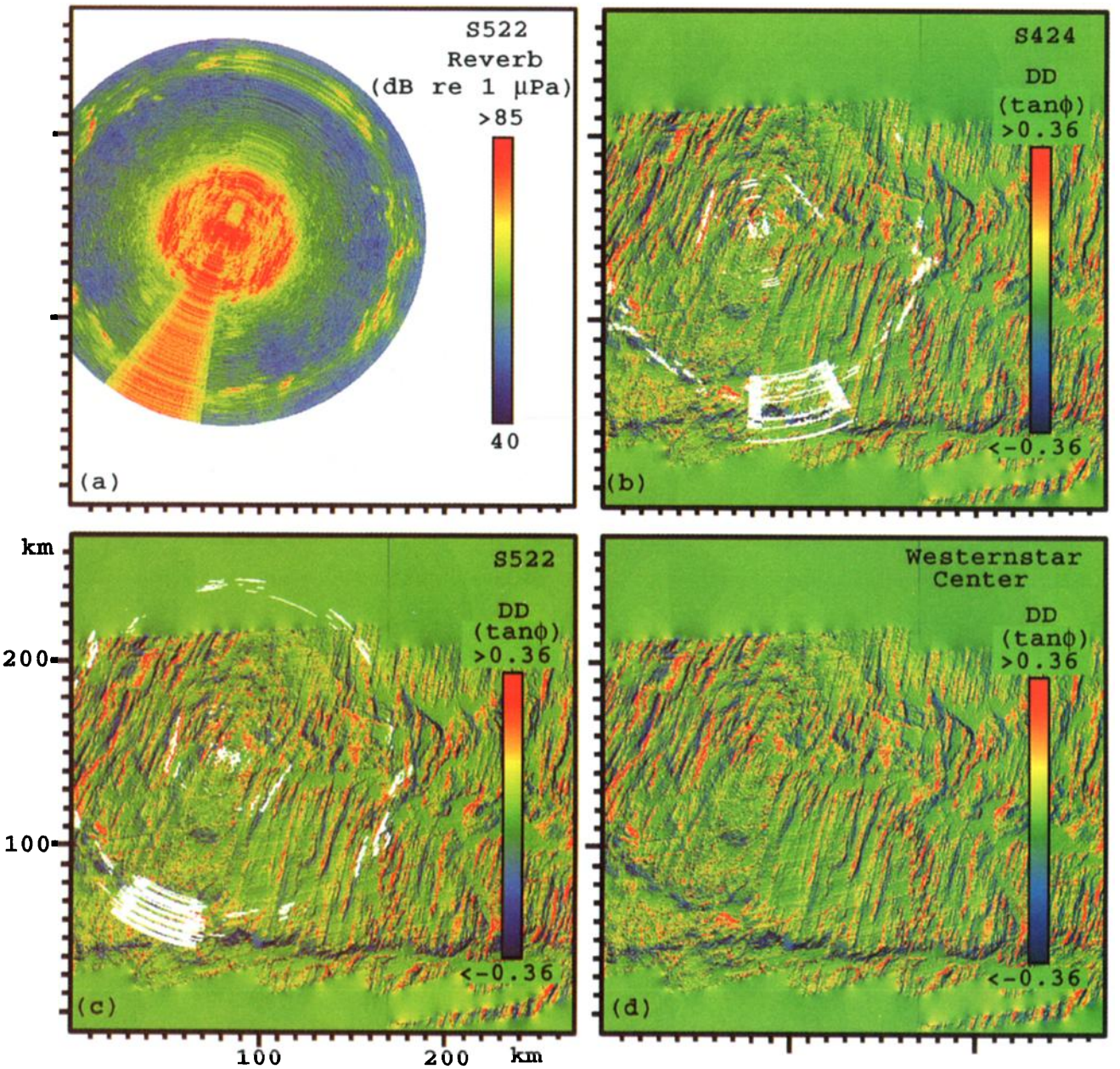

FIG. 9. (a) Same as Fig. 8 except for cw transmission s522 at receiver array heading 206°. The mean reverberation level is 61.2 dB *re*: 1 μPa, the median is 59.1 dB *re*: 1 μPa, and the standard deviation is 8.9 dB. (b) Prominent reverberation from transmission s424 (see Fig. 8 for details) in white overlain on DD with respect to the Westernstar center which is approximately the monostatic source/receiver location. Only direct-path area returns above 88 dB *re*: 1 μPa and $1\frac{1}{2}$ CZ returns above 73 dB *re*: 1 μPa are overlain. (c) Same parameters and thresholds as (b) except for cw transmission s522. (d) The directional derivative with respect to the Westernstar center without overlain reverberation.

is given in Sec. II for the relevant cw transmissions. The same convolution process was used in Ref. 3. Right–left ambiguity is also included according to the methodology of Refs. 3 and 5. The resulting quantity is actually

$$10 \log\left(\int 10 \frac{\mathrm{TL}_f + \mathrm{TL}_B}{10} \, dA \right)$$

but for consistency with the notation of Ref. 3 is denoted by $\{(\mathrm{TL}_f + \mathrm{TL}_b) - 10 \log A\}$ and is from now on referred to as blurred two-way TL. It is proportional to measured reverberation level R via the sonar equation

$$R = -\{(\mathrm{TL}_f + \mathrm{TL}_b) - 10 \log A\} + W + S, \qquad (2)$$

where W is the source level and S is the scattering strength. A map of blurred two-way TL is shown in Figs. 10 and 11 for measurements at the center of the Easternstar and Westernstar, respectively. A detailed correspondence between maxima in the reverberation chart and minima in the blurred two-way TL chart appears after comparing Fig. 6 with Fig. 10, respectively, for the Easternstar and Fig. 8 with Fig. 11, respectively, for the Westernstar.

Both measured reverberation level and modeled blurred two-way TL have approximately Gaussian statistics, as noted in the captions for Figs. 6–11. Therefore, the spatial covariance of these two logarithmic quantities provides a relatively

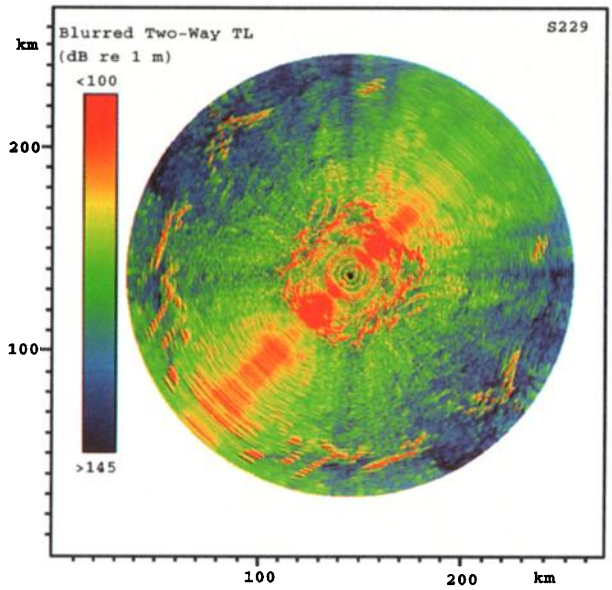

FIG. 10. A chart of modeled blurred two-way TL for the τ=0.5 s duration, f=268 Hz, cw transmission s229 over the area shown in Fig. 3. Blurring is incorporated by convolving the antilog of TL_f+TL_b with the spatially varying resolution window set by the receiving array's beamwidth and the source waveform bandwidth. Right–left ambiguity is included. A detailed correspondence between minima in this chart and measured reverberation maxima in Fig. 6 is evident, including extrema at the B′ and C′ features; an overall correlation of 0.54 is measured between the two charts. The mean level is 124.3 dB *re*: 1 m, the median is 124.6 dB *re*: 1 m, and the standard deviation is 8.7 dB. The sample probability (or histogram) for this blurred two-way TL chart has a 0.99 correlation coefficient with a Gaussian distribution of the same mean and variance.

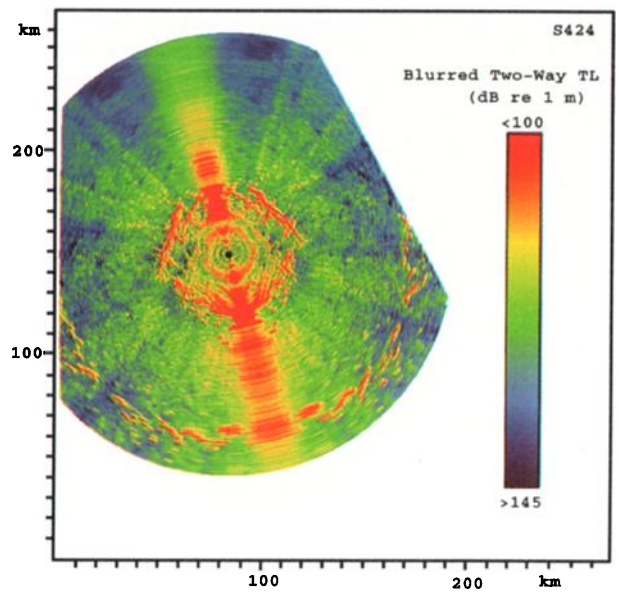

FIG. 11. A chart of modeled blurred two-way TL for the τ=0.5-s duration, f=268 Hz, cw transmission s424 over the area shown in Fig. 3. A detailed correspondence between minima in this chart and measured reverberation maxima in Fig. 8 is evident, including extrema at the B′ and C′ features; an overall correlation of 0.61 is measured between the two charts. The mean level is 124.0 dB *re*: 1 m, the median is 125.0 dB *re*: 1 m, and the standard deviation is 8.9 dB. The sample probability (or histogram) for this blurred two-way TL chart has a 0.98 correlation coefficient with a Gaussian distribution of the same mean and variance.

unambiguous measure of their dependence. (This logarithmic correlation receiver is shown in Ref. 19 to be optimal according to both information and estimation theory.) The normalized cross correlation for the measured reverberation level and blurred two-way TL charts yields a 0.54 correlation coefficient for the Easternstar (Fig. 6 vs Fig. 10) and a 0.61 correlation coefficient for the Westernstar (Fig. 8 vs Fig. 11). This is of the same magnitude as a similar correlation done for ARC data.[3] The meaning is that more than 50% of the wide-area spatial variations in measured reverberation level can be accounted for by modeled blurred two-way TL. This significant correlation quantifies the deterministic nature of

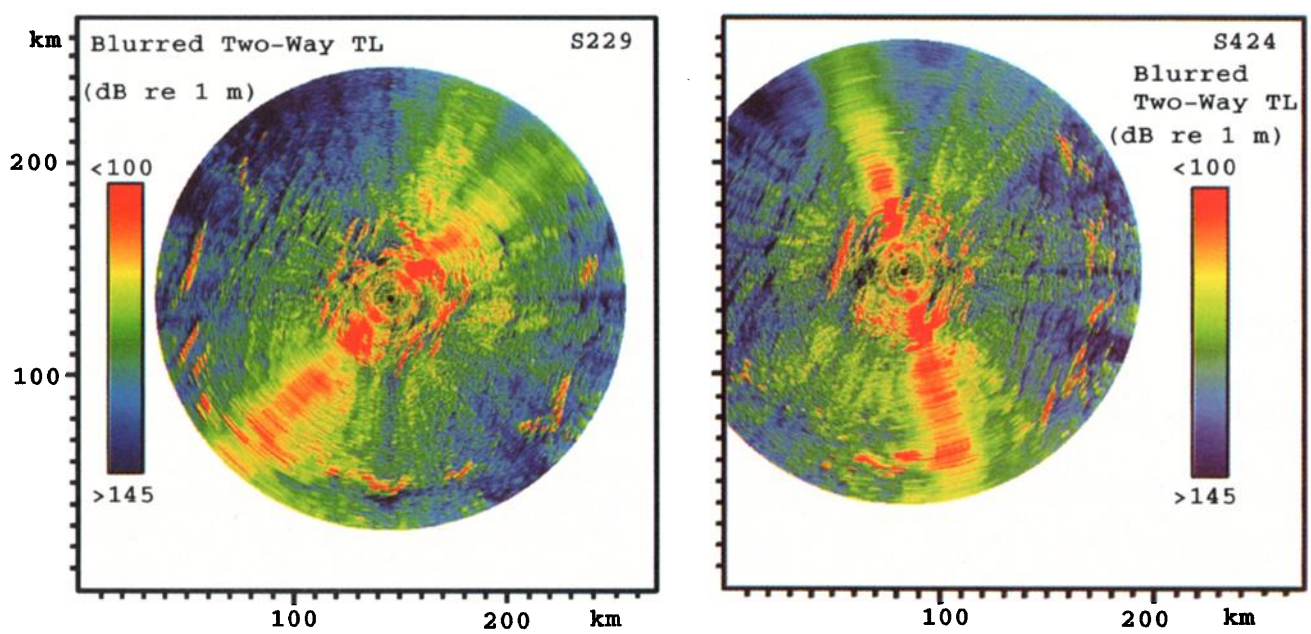

FIG. 12. Unambiguous blurred two-way TL for the segment s229 parameters given in Fig. 10 and the segment s424 parameters given in Fig. 11. These results are used in the environmental symmetry breaking ambiguity resolution technique.

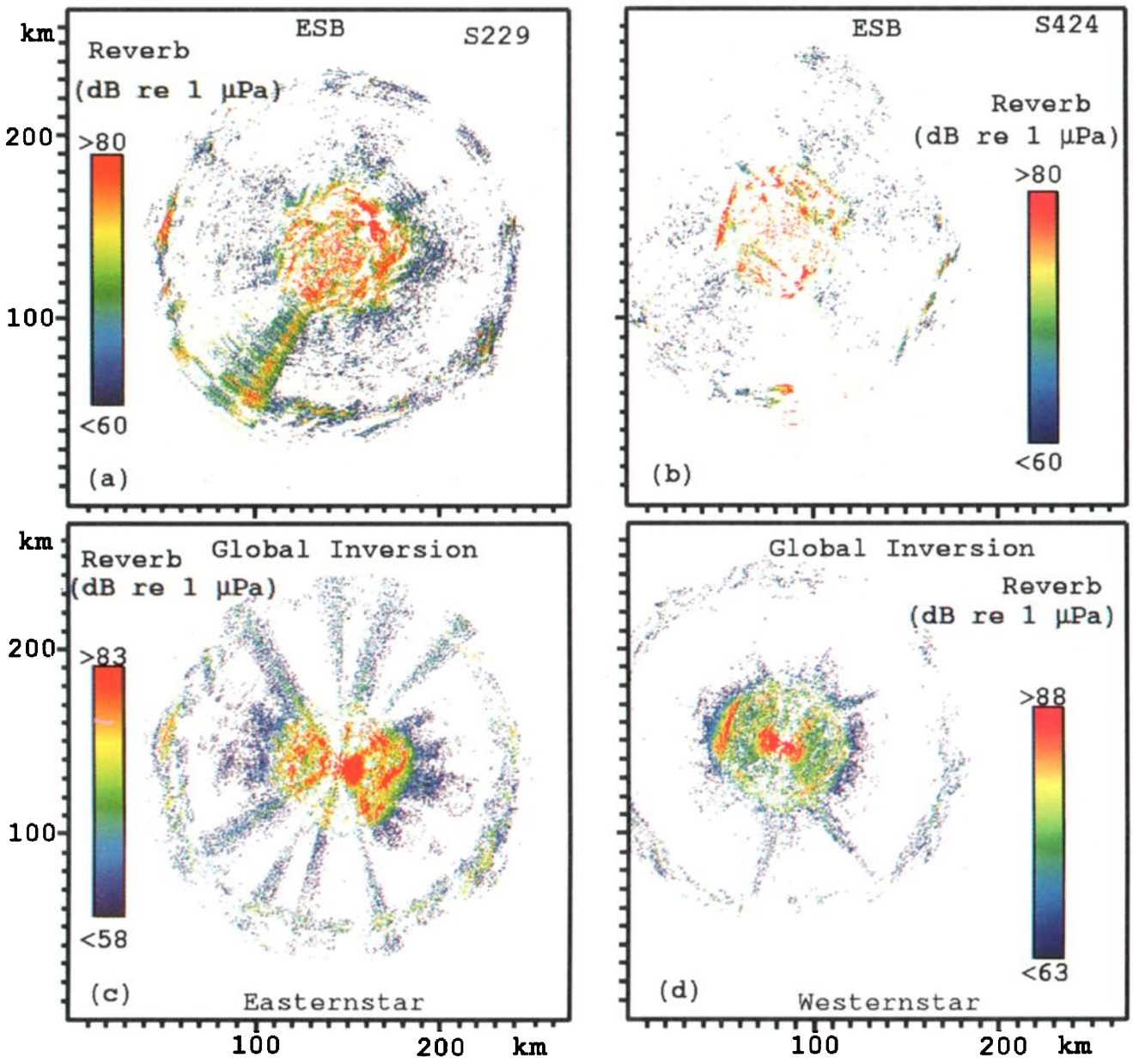

FIG. 13. Reverberation from cw transmission s229 (see Fig. 6) in (a) and cw transmission s424 (see Fig. 8) in (b) with ambiguity resolved by the ESB method. Reverberation from four Easternstar cw measurements in (c) and four Westernstar cw measurements in (d) with ambiguity resolved by the global inversion method.

the prominent reverberation. More accurate environmental data, propagation modeling, and reverberation charting will clearly improve the correlation.

IV. AMBIGUITY RESOLUTION BY TWO INDEPENDENT METHODS

A. Environmental symmetry breaking (ESB)

We first resolve ambiguity in the towed-array reverberation charts by applying the ESB technique of Ref. 3. This technique exploits known bathymetry to determine whether differences in unambiguous blurred two-way TL exist at sites where reverberation is ambiguously charted. For visual comparison, charts of unambiguous blurred two-way TL are given in Fig. 12. These correspond to the reverberation charts presented in Sec. 2 for cw measurements s229 (Easternstar) and s424 (Westernstar). In the present application of the ESB technique, the site with lower unambiguous blurred two-way TL is considered to be the true site of the return. The entire level of the return is charted to this site while nothing is charted to the ambiguous site with higher blurred two-way TL. Reverberation resolved by the ESB method is charted in Fig. 13(a) for cw measurements s229 and Fig. 13(b) for cw measurements s424. [The difference between using a 10-dB threshold (as in Ref. 3) and a 0-dB threshold (as in the present analysis) is insignificant in resolving ambiguity in the prominent reverberation of the present analysis.]

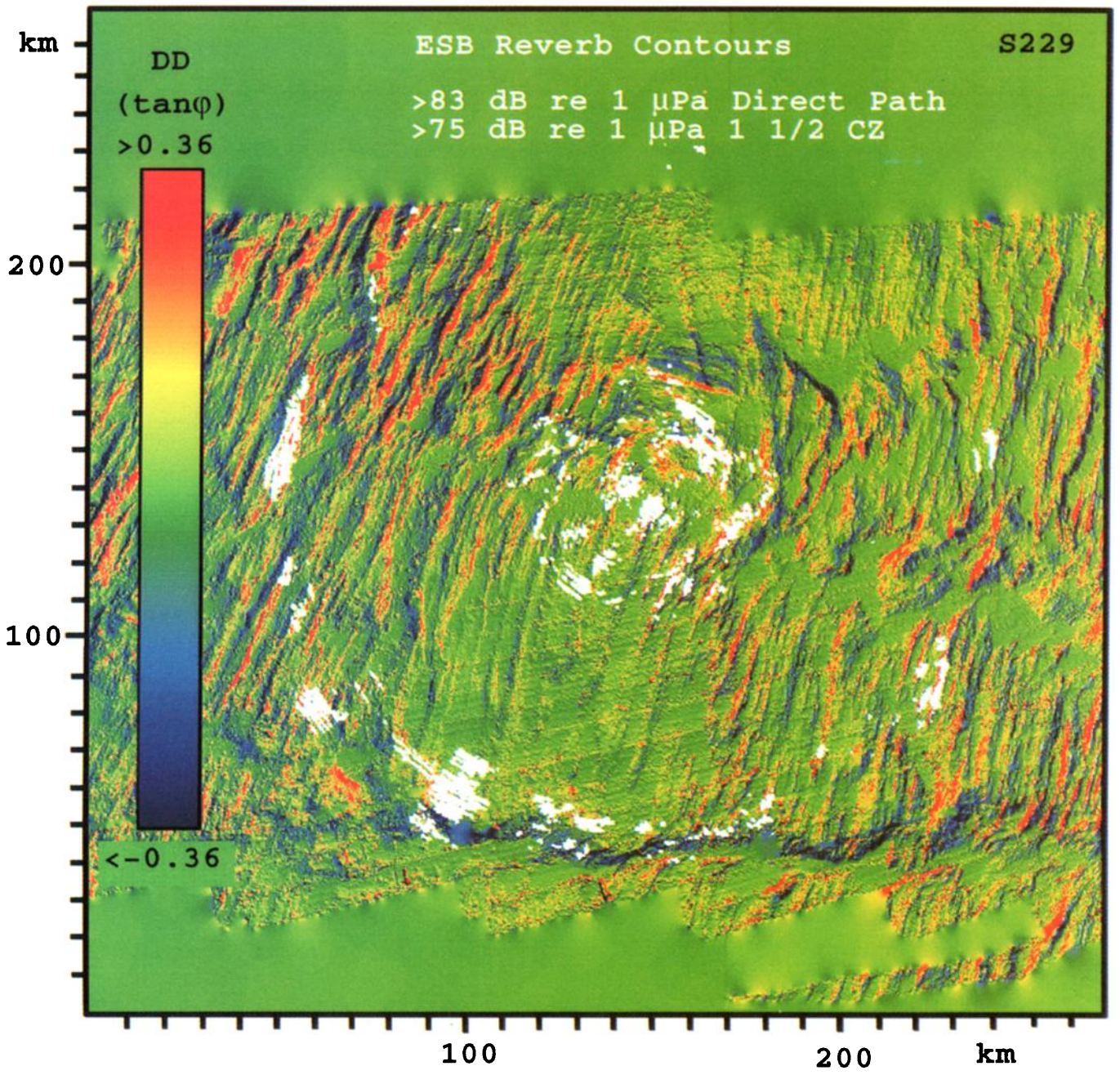

FIG. 14. White contours of prominent reverberation from cw transmission s229 resolved by the ESB method are overlain on the color DD with respect to the Easternstar center. The array heading is 224°. It is evident that prominent reverberation registers closely with and therefore returns from backfacing scarps. At endfire, resolution is too poor to resolve scarps. See Fig. 7(d) for Easternstar DD without overlay.

B. Global inversion (GI)

We next resolve ambiguity by the global inversion method described in Ref. 5. In this method, the antilog of reverberation charts from the same wide-area survey but with different array headings are simultaneously inverted by a least-squares approach. The unambiguous and optimally resolved reverberant intensity from each site in the area surveyed is the output. Here, "optimally resolved" means that the inversion attempts to resolve the reverberation from a given site to the scale represented by a pixel, even if the the local areal resolution A of the imaging system is coarser than this. This is a deconvolution process that exploits the known blurring properties of the imaging system to obtain a higher resolution and unambiguous image. The GI method is separately applied to reverberation charts from the Easternstar and Westernstar. In each case, four charts for observations made nearest the respective star center but with different array headings are used. Reverberation resolved by the GI method is charted in Fig. 13(c) for the Easternstar and Fig. 13(d) for the Westernstar.

The cw transmissions used for the Easternstar inversion (s229, s882, s918, s263 with respective array headings 224°, 344°, 179°, 28°) are all within 1.0 km of the Easternstar center, and those for the Westernstar inversion (s426, s456,

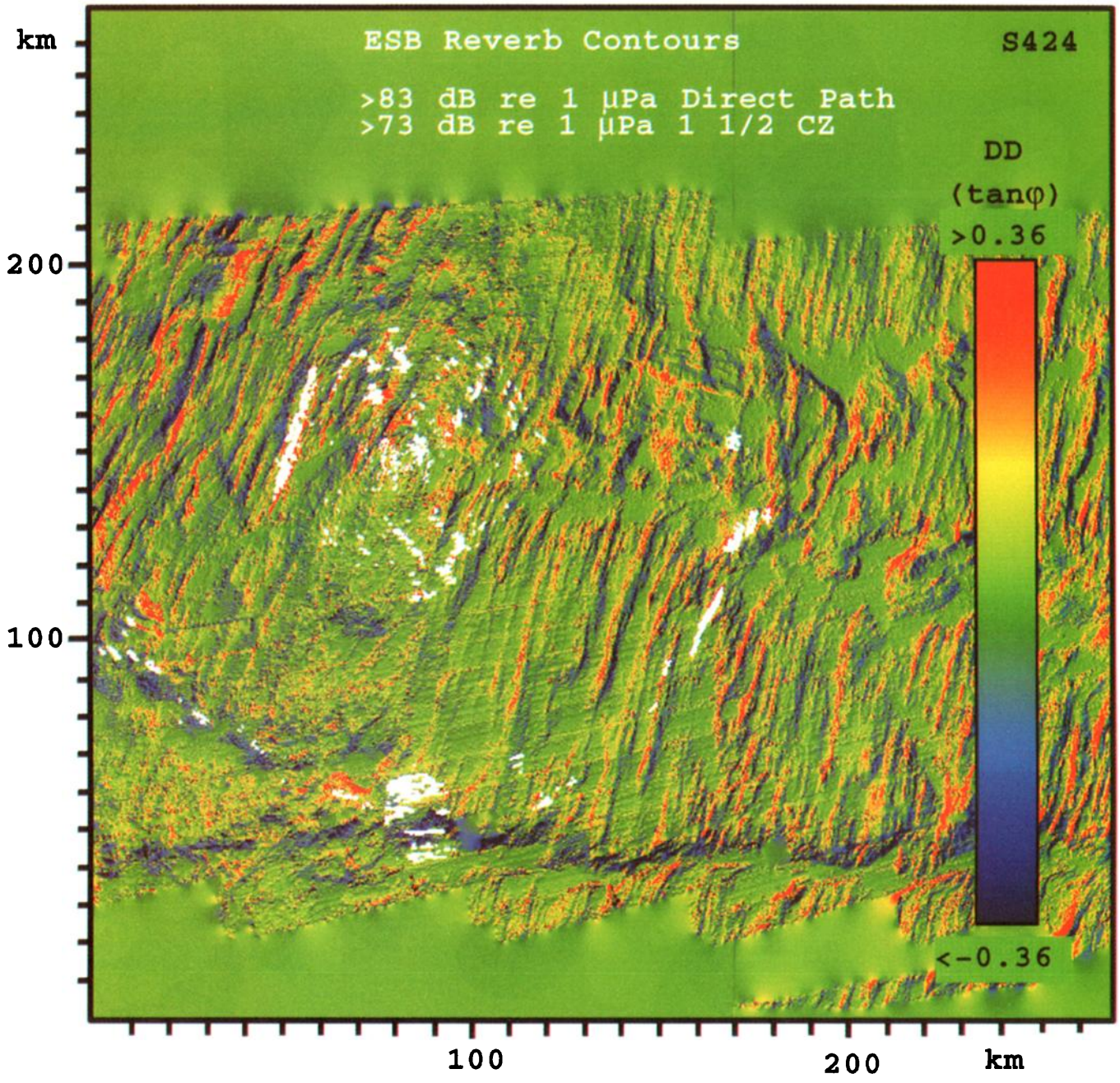

FIG. 15. White contours of prominent reverberation from cw transmission s424 resolved by the ESB method are overlain on the color DD with respect to the Westernstar center. The array heading is 168°. It is evident that prominent reverberation registers closely with and therefore returns from backfacing scarps. At endfire, resolution is too poor to resolve scarps. See Fig. 9(d) for Westernstar DD without overlay.

s487, s522 with respective array headings 168°, 1°, 44°, 206°) are all within 0.8 km of the Westernstar center. All transmissions have τ=0.5 s duration and center frequency f=268 Hz. The close proximity of the observations is intended to minimize deterministic differences caused by bathymetry-related changes in TL. (The GI method is also designed to handle measurements widely separated in space. However, in such cases, proper scaling by TL is necessary before the inversion process, and therefore only a scattering strength output is possible.)

C. Comparison

It is easiest to compare the performance of the two methods by examining the registration of prominent returns with the directional derivative of bathymetry. This is shown for the ESB method in Figs. 14 and 15 and for the GI method in Fig. 16(a) and (b).

Considering reverberation charted to $1\frac{1}{2}$ CZ, we note that backfacing scarps on B′ and C′ return strong reverberation according to both methods for respective Easternstar and Westernstar sources, and other returns are consistently charted to backfacing scarps along ridges that protrude above the excess depth contour. The location and morphology of these returns are generally consistent in both methods, and correspond to the geomorphology of ridges on the seafloor, as is evident with reference to the bathymetry in Fig. 3. By

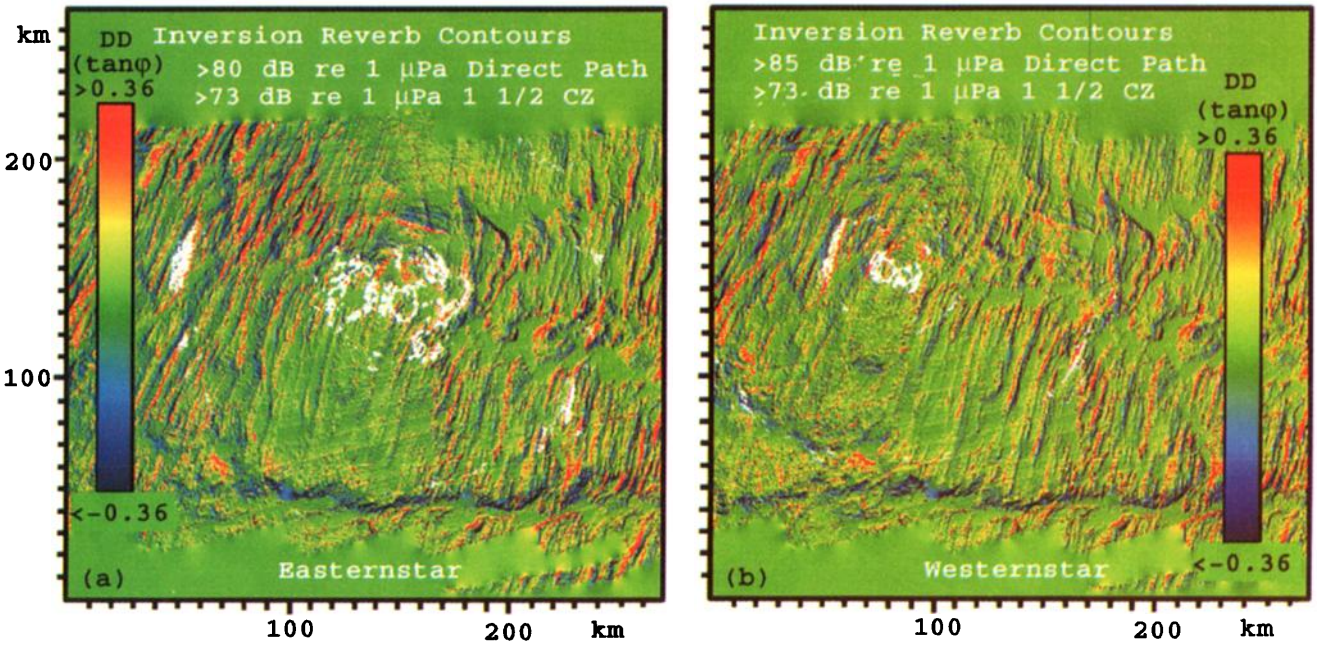

FIG. 16. (a) White contours of prominent reverberation resolved by the GI method are overlain on color DD with respect to the Easternstar center. The GI-resolved reverberation is from four monostatic cw observations made from the Easternstar center with different receiver-array headings. (b) White contours of prominent reverberation resolved by the GI method are overlain on color DD with respect to the Westernstar center. The GI-resolved reverberation is from four monostatic cw observations made from the Westernstar center with different receiver-array headings. These results show close agreement with those from the ESB technique in Figs. 14 and 15, respectively.

inspection of the direct-path area, it becomes clear that prominent returns are also charted to scarps facing the monostatic observation. For example, the B′ and C′ features return unambiguously strong reverberation according to both GI and ESB methods for Westernstar and Easternstar sources, respectively. Overall, these results are consistent with the visual ambiguity resolution and DD registration discussed in Sec. II and Ref. 12.

While the general characteristics are the same for both methods, slightly more prominent returns appear in the ESB method. This is because the GI method is only as accurate as the registration of independent reverberation charts. For example, both deterministic and stochastic differences between the measurements, as well as positioning and array orientation errors will alter the shape and number of prominent returns resolved.

D. Prominent reverberation versus bottom slope orientation

The quantitative relationship between prominent reverberation and bottom slope orientation is now documented for wide-area insonifications. Specifically, the sample probability of the DD is computed for regions where prominent reverberation above a given threshold is unambiguously charted by the ESB method. For the Easternstar reverberation chart, a threshold of 75 dB *re*: 1 μPa is used, and for the Westernstar chart, the threshold is 73 dB *re*: 1 μPa, corresponding to the thresholds used to overlay unambiguous $1\frac{1}{2}$ CZ returns in Figs. 14 and 15. However, these thresholds are now applied to the entire survey area, and no corrections are made to exclude endfire data or data between $\frac{1}{2}$ and $1\frac{1}{2}$ CZ. It is noteworthy that these thresholds are much lower than the thresholds used to overlay the unambiguous direct-path area returns in Figs. 14 and 15. The resulting DD sample probabilities are plotted in Fig. 17 along with respective cumulative sample probabilities. These curves show that roughly 60% of the prominent returns are charted to slopes facing the receiving array for the Easternstar chart. This number increases to 70% for the Westernstar chart. Increasing the reverberation level thresholds to the direct-path area threshold of Figs. 14 and 15 causes a slight increase (by 5%–10%) in these respective percentages. Similar results are obtained for the GI reverberation charts where roughly 60% of prominent returns (above 73 dB *re*: 1 μPa over the entire area) are charted to slopes facing the monostatic tow-ship observation, for either Easternstar or Westernstar locations.

For wide-area reverberation, the visual registration between prominent returns and DD in Figs. 14 and 15 can often give more insight than the sample probabilities. This is because the trained eye can deconvolve backscatter that returns from a backfacing scarp but may extend off of it in the chart due to insufficient cross range or range resolution. We believe that such insufficient resolution is the primary cause for a prominent return to be partially charted to a slope facing away from the observation, referred to as a forward facing slope or a region of negative DD. The only way to avoid this situation is to examine each scarp individually with high-resolution waveforms at broadside. This is done for the B′ ridge in Sec. VI where it is also shown how insufficient resolution can lead to the false charting of portions of a prominent return to a region of negative DD.

Close inspection of Fig. 14 indicates that certain ridges have prominent returns charted to the crest but not to lower and broader backfacing slopes. Two explanations for this are

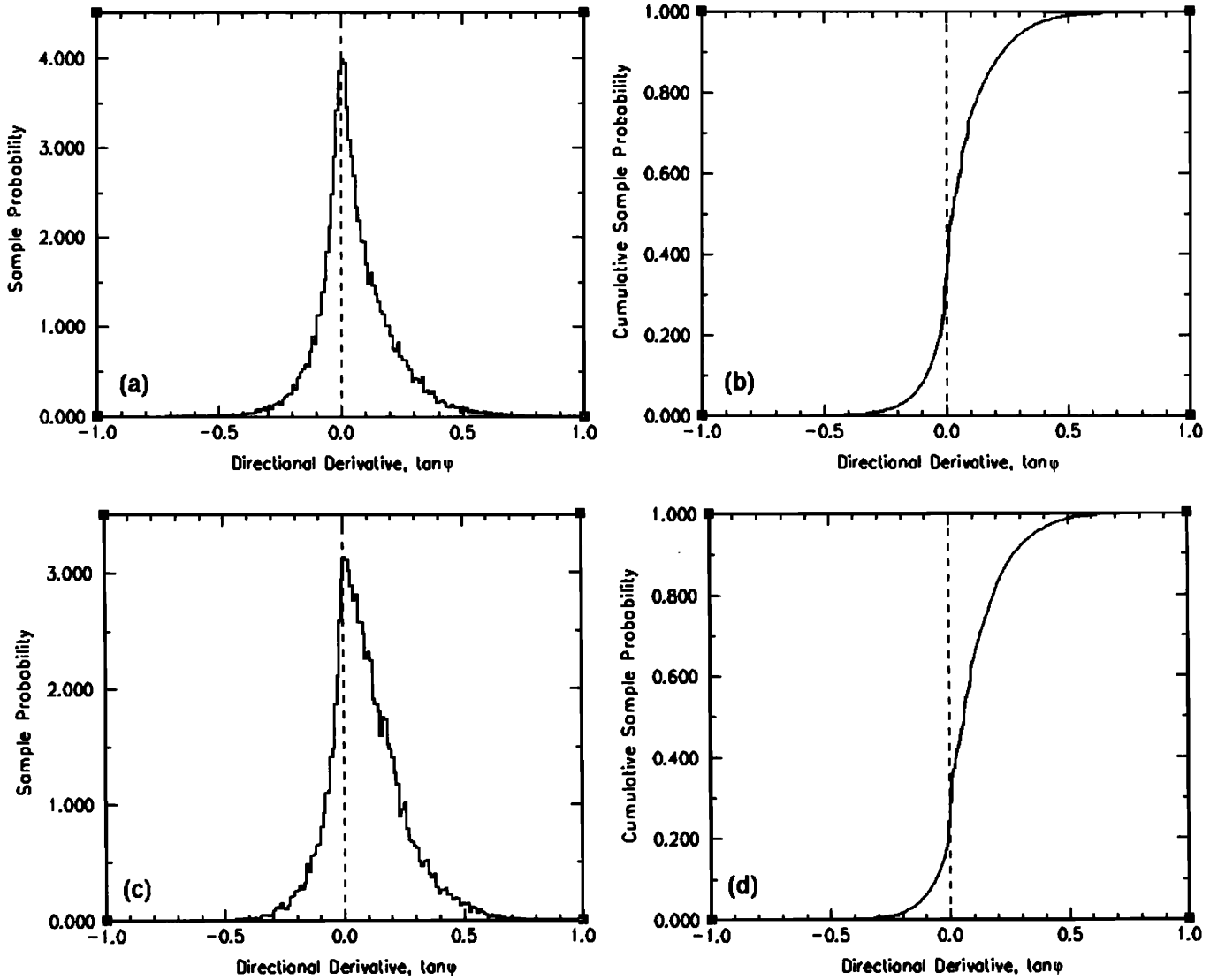

FIG. 17. (a) Sample probability for DD with respect to the monostatic source/receiver location is measured from areas where reverberation resolved by the ESB method for segment s229 is greater than 75 dB *re*: 1 μPa. The samples come from the general area of returns shown in Fig. 13(a). This encompasses the direct-path area to ranges beyond $1\frac{1}{2}$ CZ, including shadow zones and endfire. The skew towards positive DD is more apparent in (b) where the cumulative probability for (a) is shown. Specifically, roughly 60% of DD for these prominent returns is positive, indicating the primary registration is with backfacing slopes. (c) Same as (a) except for ESB-resolved reverberation greater than 75 dB *re*: 1 μPa for cw segment s424 shown in Fig. 13(b). (d) Cumulative probability for (c) where roughly 70% of DD from prominent returns is positive, indicating the primary registration is with backfacing slopes.

given: (1) When a ridge axis is at a shallow azimuthal angle with respect to the direction of propagation, the backfacing slope along the propagation radial becomes more gradual and may follow the upward refraction of the main source beam. This is the situation in the Easternstar radial shown in Fig. 18(a). Here, a modeled TL minimum is charted to the entire backface of the ridge indicated, but the strongest measured return comes from the crest in Fig. 14. We speculate that the crest returns the strongest reverberation because it contains the steepest scarps, and these scarps are not properly resolved by the Hydrosweep bathymetry and therefore do not yield the TL minima for the ridge. This effect would reduce the correlation between measured reverberation and modeled transmission loss. Higher resolution bathymetry could rectify this. (2) The insonification may only select the crests as is the case in the Easternstar radial shown in Fig. 18(b). Both of these effects would increase the probability of charting prominent returns to negative DD if the returns do not have sufficiently high-range or cross-range resolution.

V. WIDE-AREA SCATTERING STRENGTH

We combine the unambiguous blurred two-way TL charts $\{(TL_f+TL_b)-10\log A\}$ with the corresponding unambiguous reverberation charts R derived from the ESB method and scale by the source level $W=229$ dB *re*: 1 μPa at 1 m and 268 Hz to obtain spatial charts of scattering strength S for the Easternstar and Westernstar measurements. The charts are shown in Fig. 19. No apparent correlation between scattering strength and geomorphology is found, as in Ref. 3. The wide-area scattering strength sample probabilities are shown in Fig. 20, where a mean of -49 dB, a median of

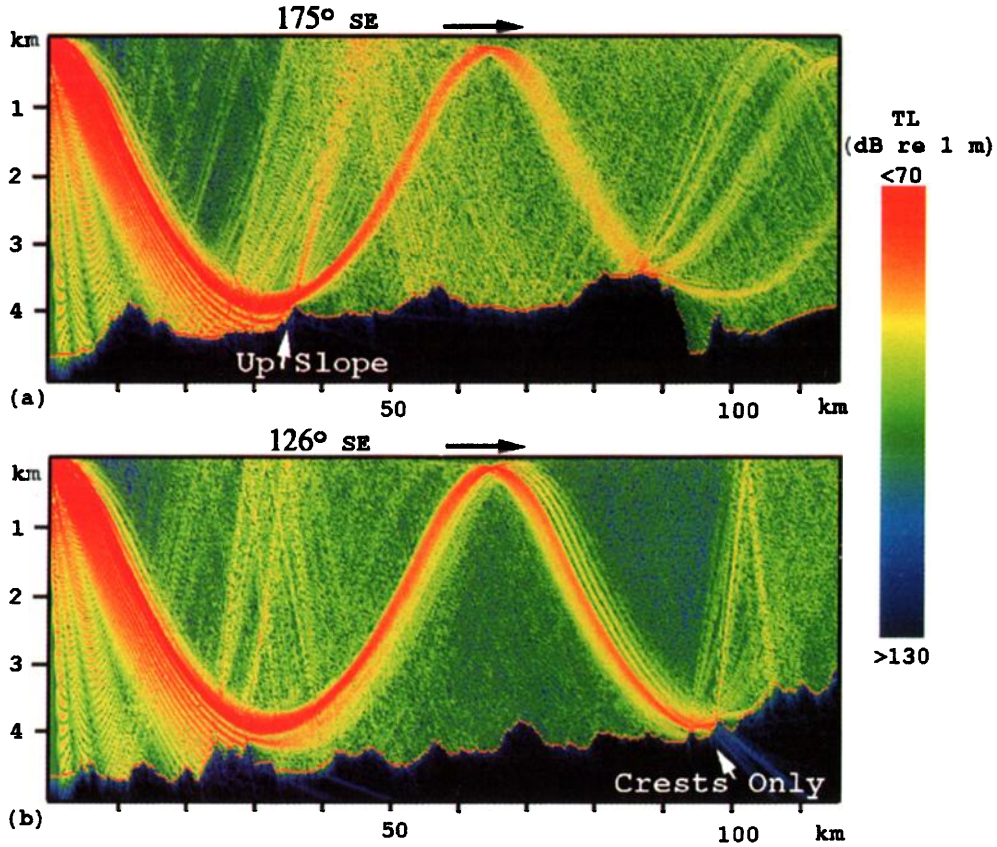

FIG. 18. Transmission loss radials from the center of the Easternstar; see Fig. 4 for modeling details. (a) This shows how upward refraction causes main-source-beam propagation up the slope of a backfacing scarp located in the direct-path area to the southeast of the Easternstar center. The upslope DD is more gradual than the local gradient of the scarp. This is because the ridge axis runs at shallow azimuthal angle with respect to the radial propagation direction. Actual returns are most prominent from the ridge crest where steeper slopes intersect the upward refracting sound. (See reverberation for cw transmission s229 or s918 charted in previous figures.) (b) This shows how waterborne propagation to scarps $1\frac{1}{2}$ CZ to the southeast of the Easternstar in cw transmission s229 insonifies only the crests.

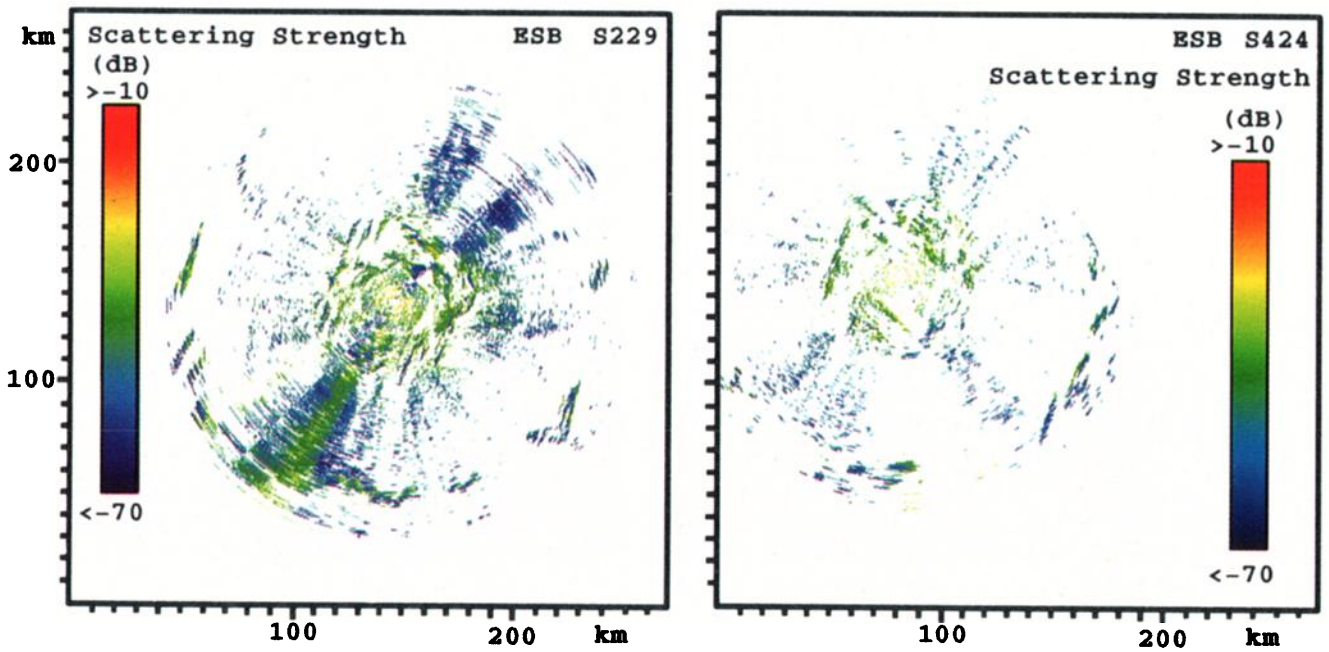

FIG. 19. Scattering strength over wide areas for cw transmission s229 and s424. The estimate is based upon reverberation charts resolved by the ESB method (Figs. 14 and 15) and unambiguous two-way TL (Fig. 12) for a source strength of 229 dB *re*: 1 μPa and 1 m.

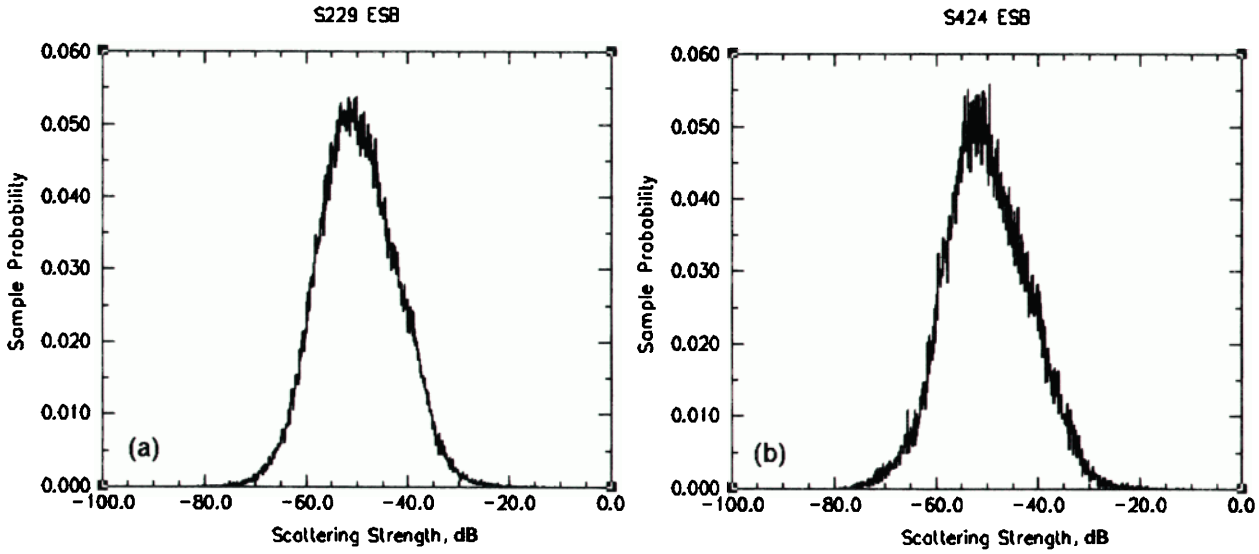

FIG. 20. Sample probabilities of scattering strength shown in Fig. 19 for (a) ESB applied to cw transmission s229 and (b) ESB applied to cw transmission s424. The −49 dB mean and 8 dB standard deviation are identical for both cases. These sample probabilities have greater than a 0.99 correlation coefficient with a Gaussian distribution of the same mean and variance.

−49 dB, and a standard deviation of 8 dB is measured for both the Easternstar and Westernstar data, consistent with ARC measurements.[3]

The standard deviation for either of the scattering strength charts is approximately equal to the individual standard deviation of any one of the reverberation charts (in captions of Figs. 6 and 8) or blurred two-way TL charts (in captions of Figs. 10 and 11). This is not surprising. While scattering strength is linearly related to reverberation level and blurred two-way TL via Eq. (2), reverberation level is shown to be highly correlated with blurred two-way TL in Sec. III, so their variances certainly do not add. Furthermore, modeled blurred two-way TL can account for the entire standard deviation of measured reverberation level. Therefore scattering strength apparently has a relatively insignificant variance when many distinct scattering contributions from wide areas are blurred together by low-resolution measurements made at long range.

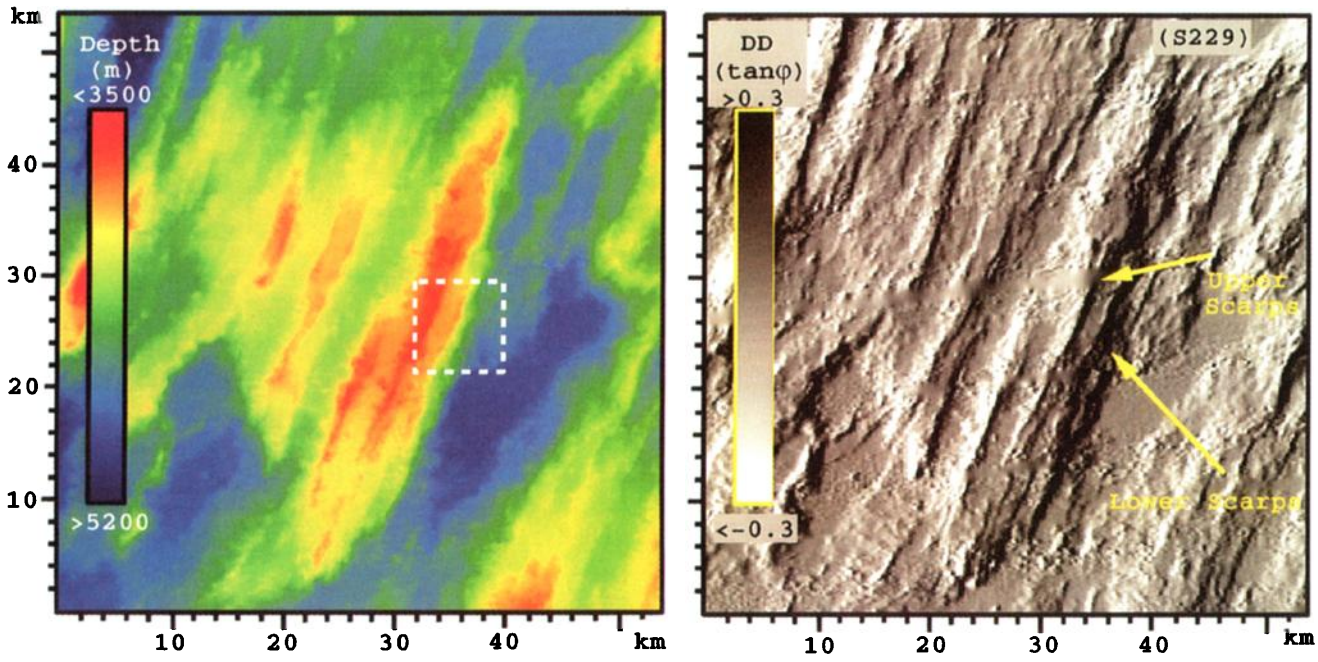

FIG. 21. (a) Hydrosweep bathymetry in the vicinity of the B′ ridge. The white box indicates the region for which fine-scale directional derivative data is presented in Fig. 22. (b) Directional derivative in the vicinity of B′ with respect to the Easternstar center from Hydrosweep bathymetry. Black indicates high positive DD (backfacing scarps) while white indicates high negative DD (forwardfacing scarps). The upper and lower scarps are identified for future reference. The Hydrosweep data presented has a 200-m horizontal resolution.

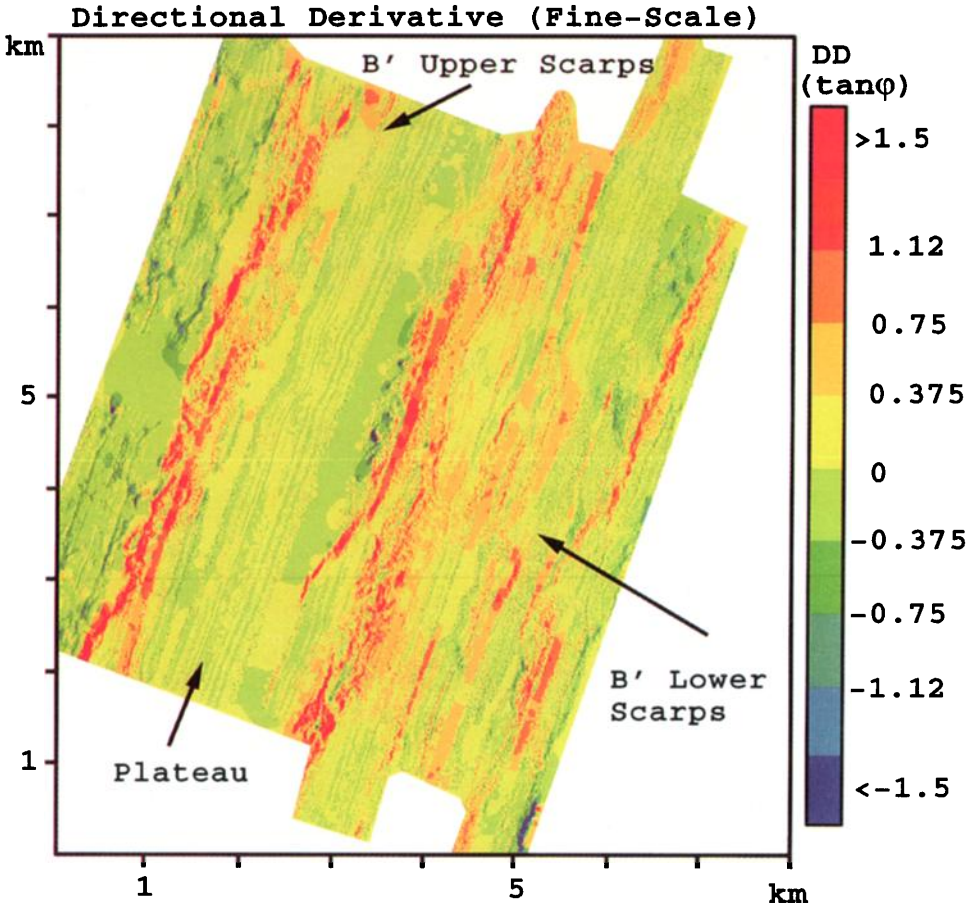

FIG. 22. Directional derivative (DD) computed from fine-scale 5-m resolution deep-tow bathymetry[23] with respect to the Easternstar center. The location of this 8 km×9 km area on B′ is shown in Fig. 21. Many steep cliffs (>60° slope) and smaller terraces (~45° slope) on both the upper and lower scarps of B′ are evident that cannot be resolved by the Hydrosweep DD of Fig. 21. Regions of blurred DD are due to interpolation of data gaps and may include 200-m sampled Hydrosweep data. Artifacts from the track of the fine-scale survey tow ship along the ridge axis are sometimes evident in the DD.

VI. COMPARING REVERBERATION FROM THE B′ RIDGE AT $\frac{1}{2}$, $1\frac{1}{2}$, AND $2\frac{1}{2}$ CZ WITH BOTTOM SLOPE ORIENTATION

In order to document the deterministic relationship between reverberation and the geomorphology of ocean ridges we examine a particular ridge. The B′ ridge is selected because its lineated scarps and plateaus extend for tens of kilometers and are easier to isolate and model than more complicated forms. The magnified bathymetry of B′ is given in Fig. 21 along with the DD with respect to the Easternstar center based upon 200-m resolution Hydrosweep data. We define the upper scarps as the eastern-facing slopes that rise to the shallowest bathymetry of B′, as indicated in Fig. 21. Directional derivatives computed from fine-scale 5-m resolution deep-tow data[23] are given in Fig. 22 for the central area over the eastern face of B′ indicated in Fig. 21. This fine-scale data reveals steep scarps that are not resolved by the lower resolution Hydrosweep DD. Analysis of the available deep-tow imagery[24] and the fine-scale DD shown in Fig. 22 indicates that the shallowest portions of the upper scarps are unsedimented cliff faces of 50°–90° slope extending about 100 m in depth from the apex of B′ and along the ridge axis for ranges between roughly 100 m to 1 km or more. Below these cliff faces are talus slopes of roughly 20°–50° inclination that extend for roughly 200–500 m to a sedimented (10–100 m thick) plateau that extends eastward for about 2 km across the ridge axis. Below the plateau are similar but generally more gradual cliffs and talus slopes, which are also indicated in Fig. 21 as the lower scarps. Both upper and lower scarps also contain some finer scale steep unsedimented cliff terraces of roughly 50° slope which extend to the bottom of the B′–C′ corridor. These terraces typically do not run exactly parallel to the axis of B′, but run along it in a discontinuous undulating pattern with a period of roughly 200 m, and have a horizontal scale of roughly 20 m in the cross-axis direction.

It is generally possible to distinguish extended scarps from ledges and plateaus even in cross range using remote measurements made at $\frac{1}{2}$ CZ range. This is because scarps and ledges are typically separated by distances greater than the 500-m cross-range resolution of the towed-array imaging systems of the RVs CORY CHOUEST and ALLIANCE at $\frac{1}{2}$ CZ. However, sheer rock cliffs and talus slopes in the scarps are typically separated by scales smaller than 500 m. Therefore, they may not always be distinguishable in a single measurement. However, it is possible that these subregions may be resolved by inverting a series of directionally independent measurements of a given scarp by a local application of the

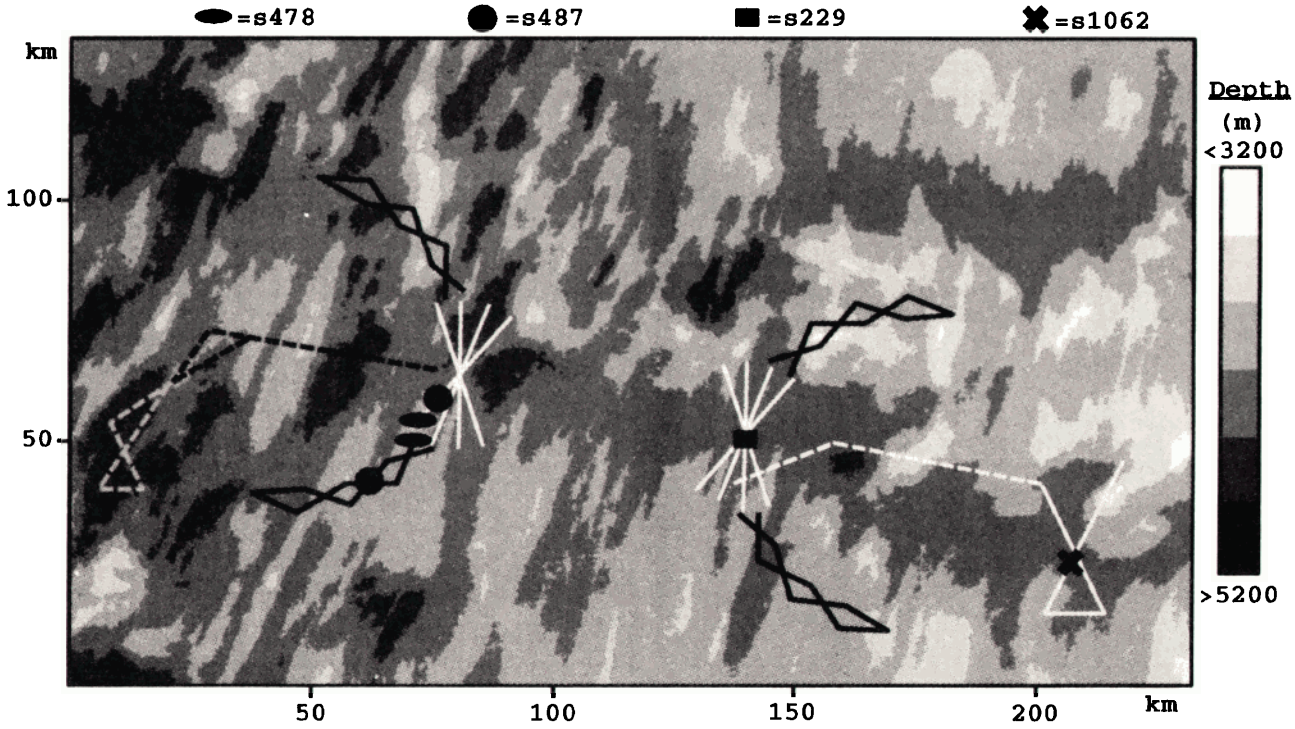

FIG. 23. Geometry of bistatic and monostatic measurements to be analyzed in Sec. VI. Ship positions are indicated by ovals (during segment s478), circles (during segment s487), squares (during segment s229), and an × (during segment s1062). White lines indicate RV CORY CHOUEST while black and grey indicate RV ALLIANCE tow-ship tracks. Note that s478 and s487 are transmitted by the RV CORY CHOUEST and received by both the RV CORY CHOUEST and ALLIANCE at the indicated points.

global inversion. Furthermore, we believe that the expected directional dependence and magnitude of scattering from a given scarp can be empirically parametrized as a function of the bistatic measurement geometry and the mean orientation of the scarp. Such a parametrization goes beyond the scope of the present analysis. However, with the illustrative examples of this section, we show that such a parametrization would be useful because the relationship between steep

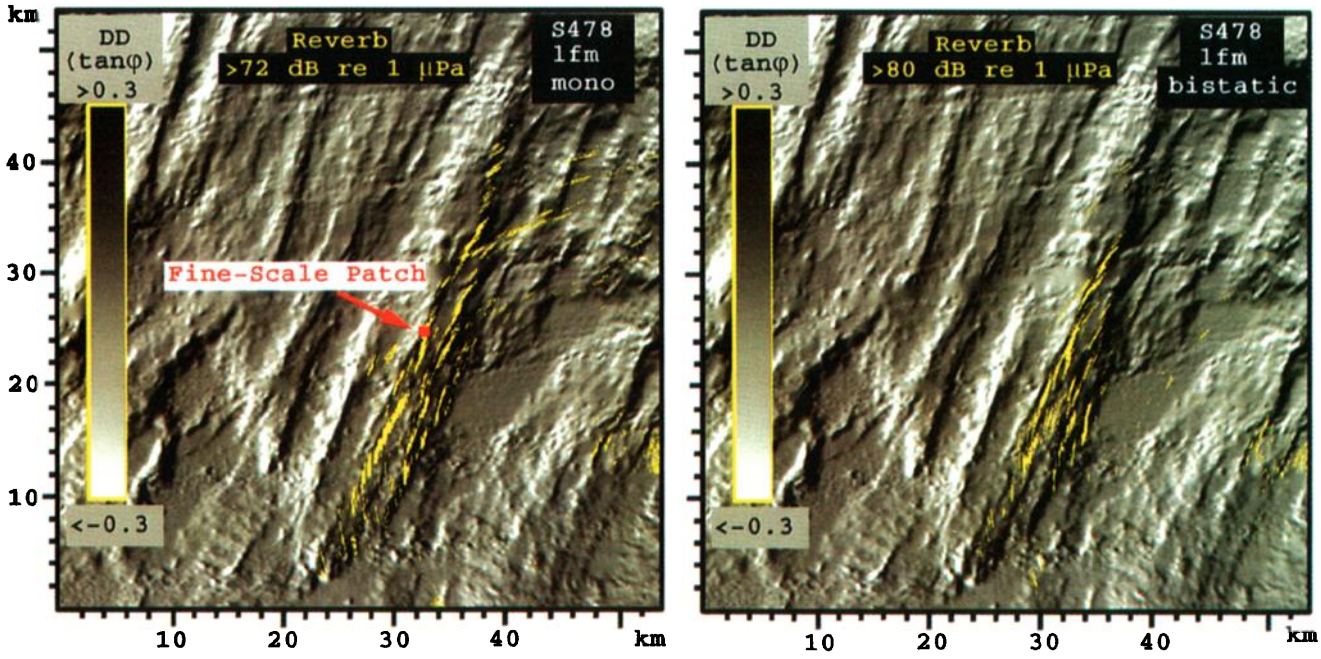

FIG. 24. Prominent monostatic and bistatic reverberation measured from B′ at roughly 1/2 CZ for LFM transmission s478 (over the frequency band f=200–225 Hz) is overlain in yellow on the black and white DD with respect to the receiving-array location. The RV CORY CHOUEST is the receiver for monostatic, and the RV ALLIANCE is the receiver for bistatic measurements. Prominent returns show close registration with receiver-facing scarps. This is for the same area as in Fig. 21. Similarity in mono- and bistatic returns is due to the close proximity of the source and receiver; see Fig. 23 for geometry. A 1×1 km box is identified for comparison between reverberation shown and fine-scale (5-m resolution) DD in Fig. 26.

scarps and prominent reverberation is deterministically related to the bistatic orientation of the measurement with respect to the axis of the given scarp.

We apply neither the ESB nor the GI ambiguity resolution methods to the data presented in this section. This isbecause the track design has exploited the bathymetry to provide overwhelmingly unambiguous returns from B′ for the specific segments to be analyzed. [However, this is not the case for all Westernstar segments, as can be seen in Figs. 8 and 9 where ambiguous returns are charted across the B′ ridge axis for cw transmission s424. These ambiguous returns are successfully removed by both ESB and GI, as shown in Figs. 15 and 16(b).]

A. Monostatic and bistatic reverberation within the direct-path area

The geometry of the monostatic and bistatic measurements to be analyzed in this section is indicated in Fig. 23. We begin with reverberation at roughly $\frac{1}{2}$ CZ from the B′ ridge for a $\tau=5$ s duration LFM transmission in the frequency band 200–255 Hz. The nominal range resolution for bandwidth $B=55$ Hz is $\Delta r=c/(2B)=13.6$ m. Such high-range resolution is unnecessary for this analysis because of (1) the roughly 100-m accuracy of the GPS navigation presently being used, (2) the roughly 200-m resolution of the Hydrosweep bathymetry used in the charting, and (3) the 54 km by 54 km area of our reverberation charts around B′. Including the time averaging discussed in Sec. II to reduce the standard deviation of the measurement, we employ an effective range resolution of roughly $\Delta r=cT/2=47$ m for RV CORY CHOUEST receptions and $\Delta r=42$ m for RV ALLIANCE receptions. Prominent returns for LFM transmission s478 are overlain on the Hydrosweep DD of B′ and vicinity in Fig. 24. These prominent returns are clearly charted to regions of high DD associated with steep scarps facing the observation. The scarps that yield prominent returns are very similar when the transmission is measured monostatically by the CORY, and bistatically by the ALLIANCE. This is due to the small separation between the CORY and the ALLIANCE[25] for this segment (shown in Fig. 23) and the resulting small bistatic separation between the incident and scattered angles in azimuth. (Reference 26 provides a useful and contemporary discussion of bistatic reverberation charting issues, although for much longer range and lower resolution returns than those of the present study.)

The incident direction of sound is always near normal incidence to the central east-facing B′ escarpments because the CORY is always in the Westernstar during the transmissions analyzed in this section. Quantitative confirmation of the deterministic relationship between prominent reverberation and scarps facing the receiver is given by the DD sample probabilities for the monostatic case in Fig. 25(a) and (b) and for the bistatic cases in Fig. 25(c)–(f). Here roughly 90% of the reverberation returns from slopes facing the receiver, and roughly 50% returns from slopes facing the receiver with Hydrosweep DD greater than 10°. (These results are essentially unchanged for linear, slant-range and ray-trace charting.) It is important to note that the 200-m bathymetric sampling used to compute the Hydrosweep DD is on the order of the resolution of the reverberation measurement. This may be adequate to indicate some of the larger cliffs, but not to give an accurate estimate of their slope nor to resolve the finer scale cliff terraces observed on the upper and lower scarps of B′. For example, the fine-scale DD of Fig. 22 shows that these cliffs and small scale terraces have significantly higher slope than can be resolved by the Hydrosweep DD over the same area. When insonified, these steep cliff terraces may make the dominant contribution to the mean reverberation measured in a given resolution area ($A=r\Delta r\beta$). Therefore the sample probabilities of Fig. 25 may be skewed even further towards high DD if fine-scale bathymetry is used.

An example of a region with large cliffs and terraces that returns strong reverberation is shown in Fig. 26, where the fine-scale 5-m resolution bathymetry is used to compute DD. The same 1×1 km region is indicated in Fig. 24, where a prominent return is clearly charted. White boarders containing prominent monostatic reverberation for LFM transmission s478 are indicated in Fig. 26 for the respective threshold of Fig. 24. These boarders span roughly ten times our working range resolution of $\Delta r=47$ m for the given monostatic LFM transmission. With this thresholding, the range extent of the return is closer to the resolution of the Hydrosweep bathymetry. Higher resolution comparisons, approaching Δr, are left for a future paper. The purpose here is to explicitly show that (1) a significant amount of spatial averaging is done by the towed-array imaging system over the varying geomorphology of a representative scarp, and (2) the scarp yielding the prominent return actually has steep slopes of 60°–90° and not the far more gradual 20°–30° slopes estimated from the lower resolution Hydrosweep bathymetry. We hypothesize that most prominent returns in the area come from such steep cliffs, and plan to quantitatively document the relationship between fine-scale DD and reverberation level to test this hypothesis. Furthermore, because the cliffs and terraces that register with the prominent return in Fig. 26 are significantly larger than a wavelength, we believe that (1) the Kirchhoff approximation may provide a useful model of the local scattering, and (2) the mean scattering resolved by the towed-array imaging system may be Lambertian. (Forward scattering from B′ is generally excluded by the measurement geometry, except in run 6 where an attempt is made to isolate this effect and to determine the relative importance of diffraction.[10])

Prominent reverberation from LFM transmission s487 is shown in Fig. 27. Here, the bistatic separation between the CORY and ALLIANCE has increased significantly with respect to that for segment s478. The monostatic returns are similar to those for LFM transmission s478 except at the southern part of B′. Here the cross-range resolution is no longer along the scarp axis, but runs noticeably diagonal. This tends to falsely extend prominent returns in cross range to level sedimented areas and regions of negative DD, where such prominent reverberation would otherwise not be charted. However, it also provides much higher resolution of anomalous cliffs, that must run skew of the scarp axis to face the receiver, than is possible when cross range is oriented along the scarp axis. This is because the range resolution is on the order of 50 m

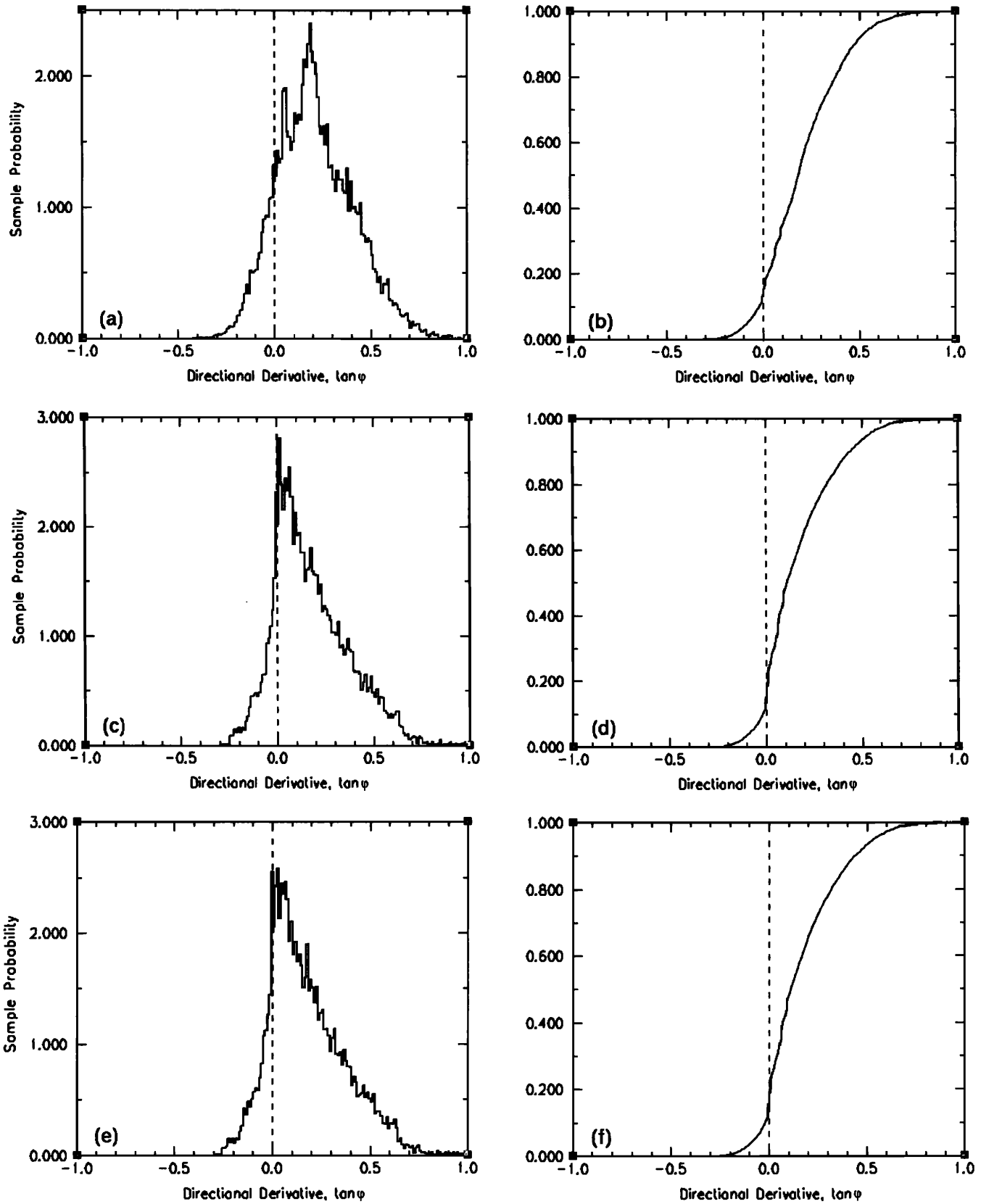

FIG. 25. Sample and cumulative sample probabilities for DD in areas where prominent reverberation is shown in Fig. 24. All sample probabilities show a large skew toward positive DD. All cumulative sample probabilities show that roughly 90% of DD is positive, indicating an overwhelming portion of prominent returns come from source/receiver-facing scarps on B′. The (a) DD sample probability and (b) cumulative sample probability with respect to the Cory's monostatic source/receiver location for prominent returns (>72 dB *re*: 1 μPa) for LFM transmission s478. (c) The DD sample probability and (d) cumulative sample probability with respect to the Cory's source location for prominent bistatic returns (>80 dB *re*: 1 μPa) for LFM transmission s478. Both (e) and (f) are the same as (c) and (d) but for DD with respect to the Alliance's receiver location.

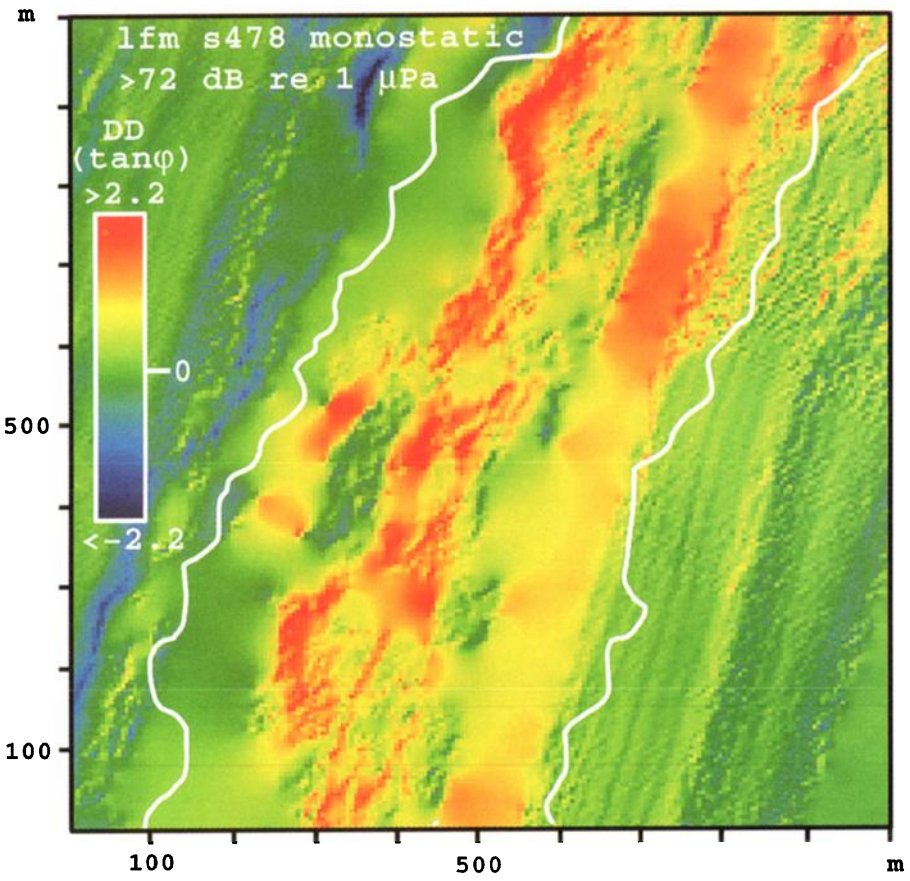

FIG. 26. White contours indicate the region within which prominent monostatic reverberation (>72 dB *re*: 1 μPa) from B′ at roughly $\frac{1}{2}$ CZ is charted for LFM transmission s478. These contours are overlain on the color DD with respect to the receiving-array location. The DD is computed from fine-scale 5-m resolution bathymetry. The location of the 1×1 km box on B′ is shown in Fig. 24. The purpose of this figure is to illustrate how scattering from many steep cliffs (>60° slope) and smaller terraces (~45° slope) on a typical scarp is averaged (blurred) over the areal resolution of the towed-array system for a given prominent return. Regions of excessively smoothed DD are due to interpolation of data gaps and may be filled with 200-m sampled Hydrosweep data. Artifacts from the track of the fine-scale survey tow ship along the ridge axis are sometimes evident in the DD.

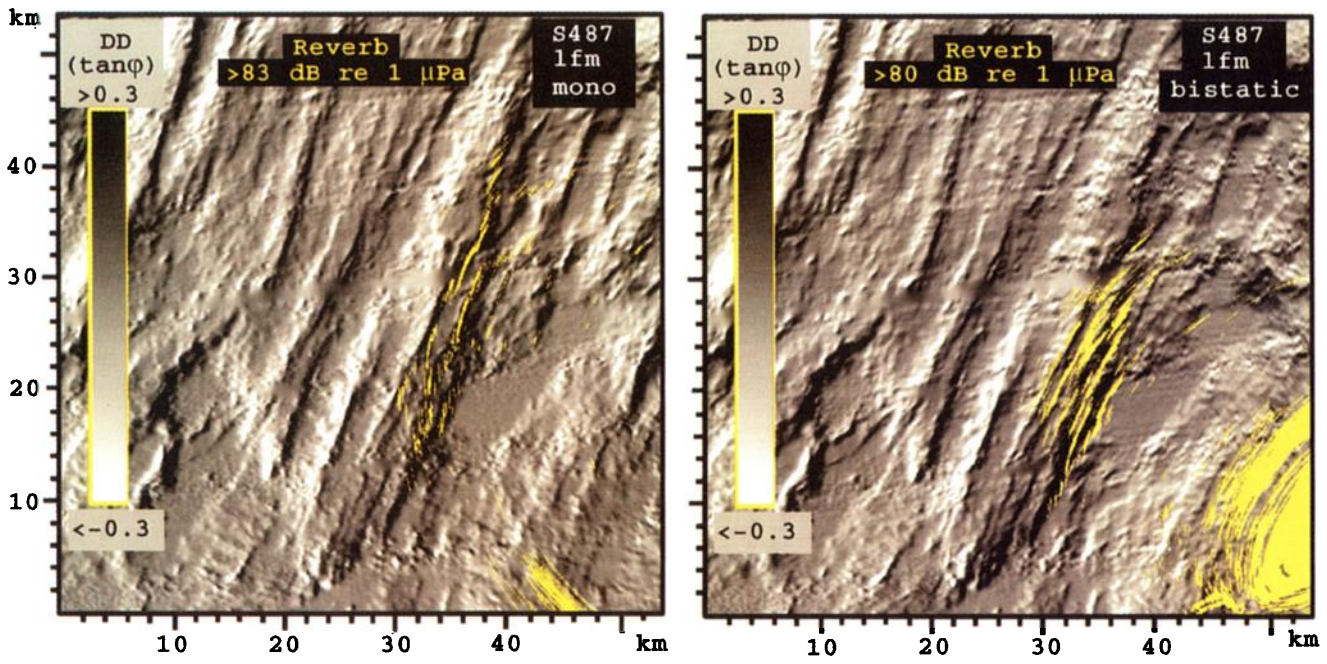

FIG. 27. Same as Fig. 24 except using LFM transmission s487. The bistatic separation between the CORY and the ALLIANCE has increased significantly and the prominent mono- and bistatic returns come from significantly different locations on the backfacing scarps of B′.

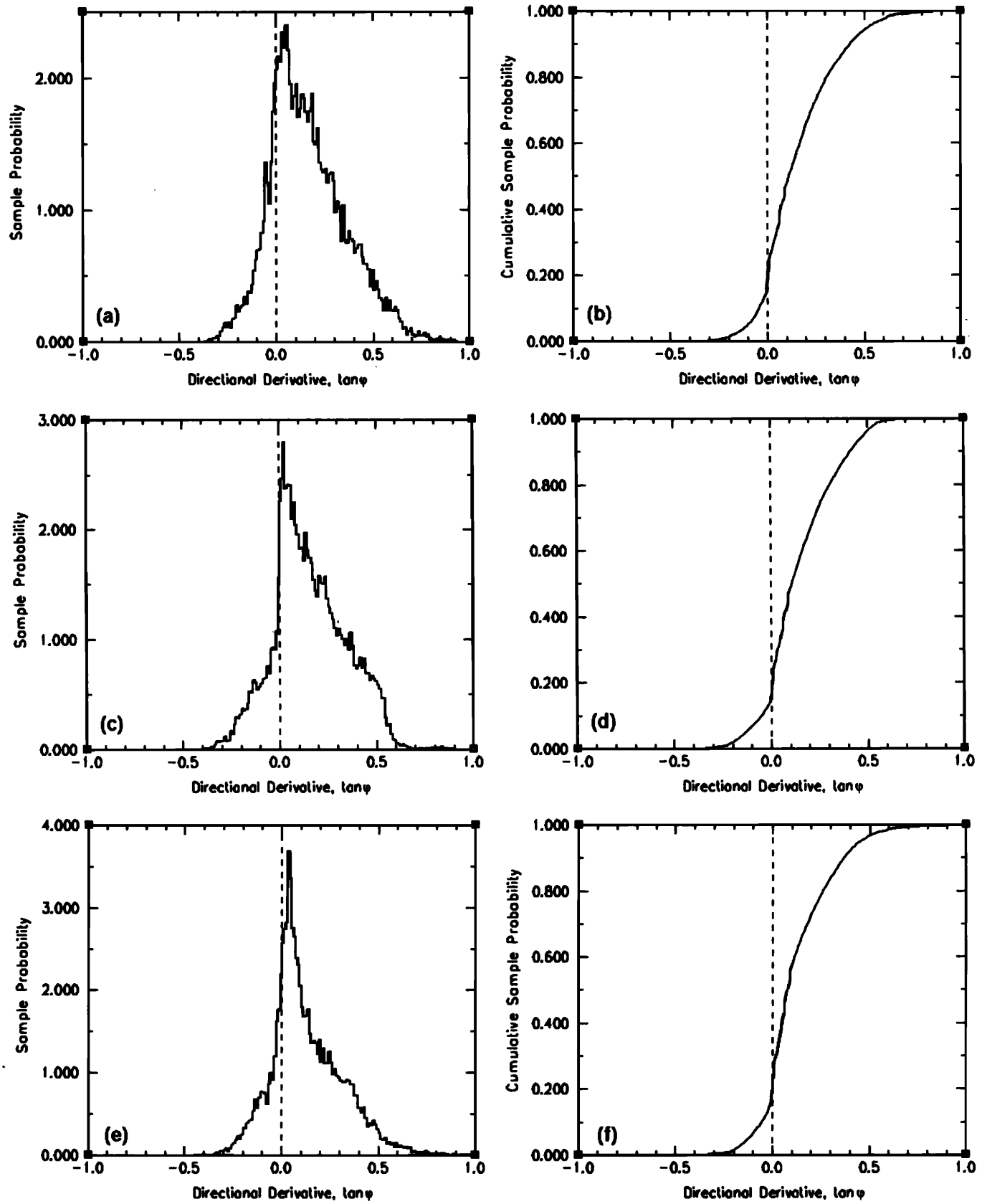

FIG. 28. Same as Fig. 25 except using LFM transmission s487. Again roughly 90% of DD is positive, indicating that an overwhelming portion of prominent returns come from source/receiver-facing scarps on B′. (a) The DD sample probability and (b) cumulative sample probability with respect to the Cory's monostatic source/receiver location for prominent returns (>83 dB *re*: 1 μPa) for LFM transmission s487. (c) The DD sample probability and (d) cumulative sample probability with respect to the Cory's source location for prominent bistatic returns (>80 dB *re*: 1 μPa) for LFM transmission s487. Both (e) and (f) are the same as (c) and (d) but for DD with respect to the Alliance's receiver location.

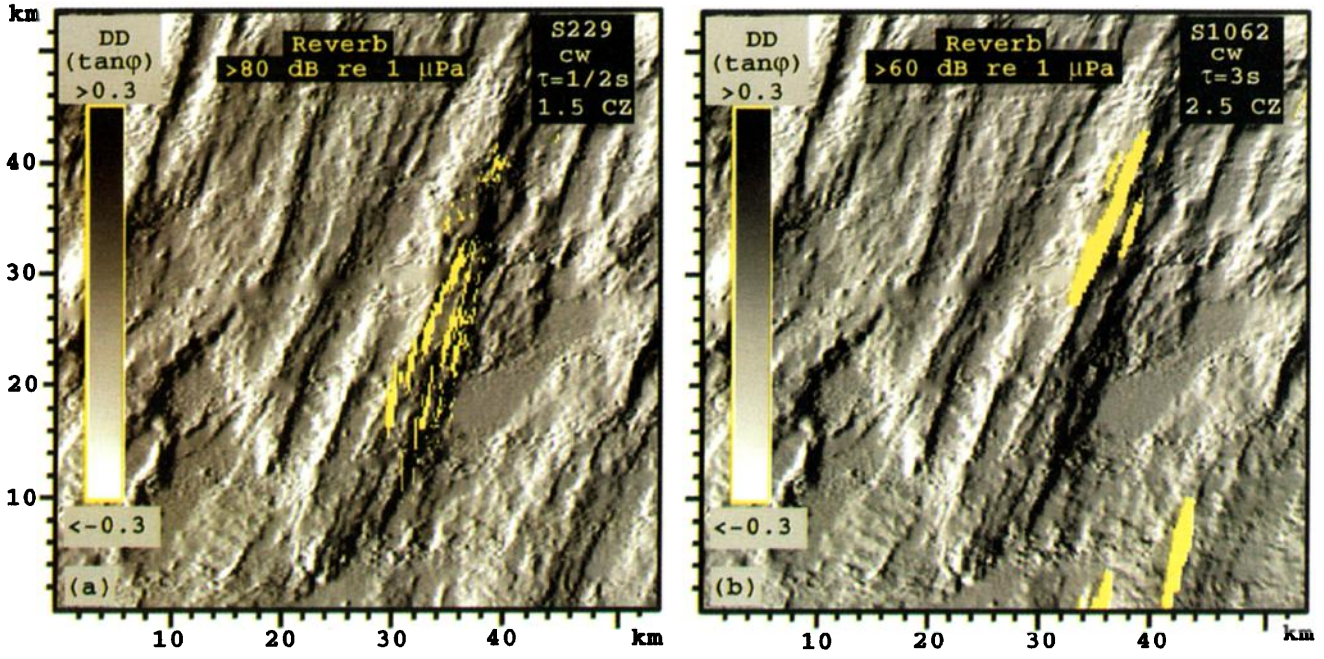

FIG. 29. (a) Prominent monostatic reverberation measured from B′ at $1\frac{1}{2}$ CZ for cw transmission s229 is overlain in yellow on the black and white DD with respect to the Cory's monostatic source/receiver-array location. Prominent returns show close registration with backfacing scarps just as at $\frac{1}{2}$ CZ in Figs. 24 and 27. (b) Prominent monostatic reverberation from B′ at $2\frac{1}{2}$ CZ for cw transmission s1062 overlain on the DD with respect to the Cory's monostatic source/receiver-array location. Linear conversion from travel time to range is used. The increased pulse duration causes returns from the upper scarp to extend behind the crest in linear charting. This is consistent with the zero-range/zero-start-time of the pulse. This example shows how decreased resolution in range and cross range can degrade a quantitative correlation between positive DD and prominent returns.

and the cross-range resolution is typically 10× this. The bistatic reverberation for LFM transmission s487 is clearly different from the monostatic. This is due to the significant bistatic separation between the CORY and the ALLIANCE that approaches roughly 30° with respect to the center of B′. (The center of B′ is where the ALLIANCE track runs over the upper scarp in Fig. 23.) Specifically, scarps with high DD again return the strongest reverberation, but the DD for this ALLIANCE position is considerably different from that in segment 478. The DD probabilities for LFM transmission s487 shown in Fig. 28 confirm the strong quantitative relationship between positive DD and reverberation.

B. Backscatter from $1\frac{1}{2}$ and $2\frac{1}{2}$ CZ

A magnification of B′ backscatter is given in Fig. 29(a) for the τ=0.5-s duration, Δr=375 m resolution, cw transmission s229 first presented in Fig. 6. Once again a strong relationship is evident between scarps facing the monostatic observation and prominent returns. The DD sample probabilities of Fig. 30(a) and (b) again show that roughly 90% of prominent returns are charted to scarps facing the tow ship. However, this is from $1\frac{1}{2}$ CZ or roughly 100 km away! (See Fig. 23 for the exact geometry.) This demonstrates that low-frequency towed-array systems can be used to remotely image a specific ridge with horizontal resolution approaching that of traditional ship-mounted sidescan sonar. For example, the towed-array image of the backfacing scarps on B′ shown in Fig. 29(a) approaches the resolution of Hydrosweep DD that it is overlain upon.

To illustrate the issues involved in comparing low-resolution reverberation with much higher resolution bathymetry, we consider the returns from B′ measured at 2 $\frac{1}{2}$ CZ or roughly 167 km away as indicated in Fig. 23 for segment s1062. These returns are obtained for a τ=3-s duration, Δr=2.25-km resolution cw transmission. Prominent reverberation is overlain upon DD in Fig. 29(b). A linear charting procedure is used, as in Ref. 3. Therefore returns from the upper backfacing scarp extend significantly beyond the apex of B′ to westerly regions of negative DD as a consequence of the 3-s pulse duration. (The zero time/range reference is with respect to the onset of the transmission. Therefore, only the onset of the pulse is charted to the backfacing scarp due to poor range resolution.) Reduced cross-range resolution is also evident as a smearing of the return over the respective scarp face. These observations are quantitatively confirmed by the sample probabilities of Fig. 30(c) and (d). These show that resolution is too poor to distinguish back- from forward-facing scarps on the B′ ridge. Extrapolating these results, it is evident that as the scale of the cliff faces and resolution of the bathymetry becomes much finer than the resolution of the reverberation, false charting of this kind will eventually occur. This situation is anticipated in future comparisons between LFM returns and fine-scale cliffs and terraces on the B′ scarps. The use of a ray trace instead of a linear or slant-range charting procedure prevents such false charting to some extent.

VII. CONCLUSIONS

We present initial results of an ocean-basin reverberation experiment conducted over the western flank of the Mid-Atlantic Ridge (MAR). The experiment is known as the Main Acoustics Experiment (MAE) and is part of an Office

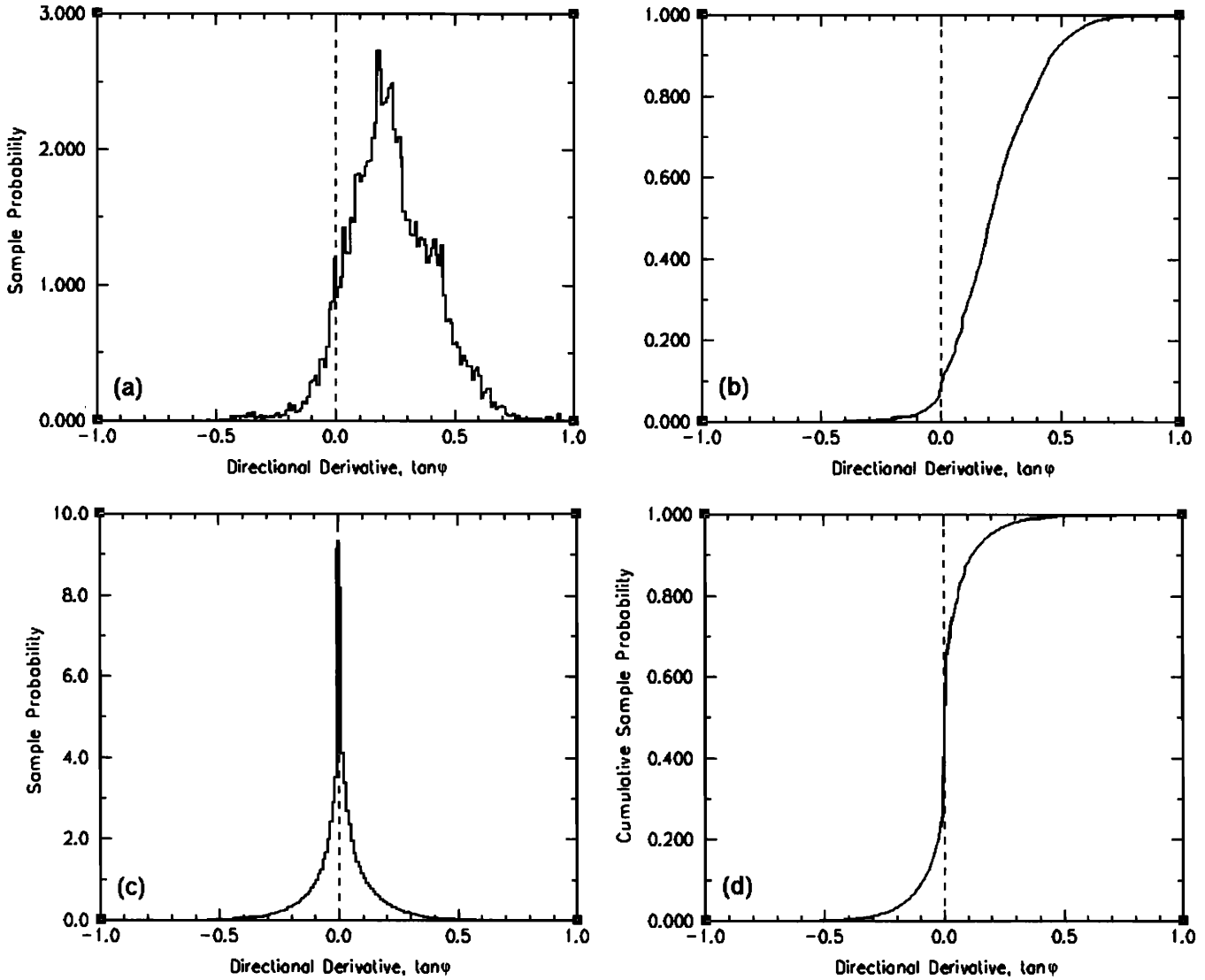

FIG. 30. (a) The sample probability and (b) cumulative sample probability for DD with respect to the Cory's monostatic source/receiver location over areas where prominent monostatic returns (>80 dB *re*: 1 μPa) are charted for cw transmission s229 at $1\frac{1}{2}$ CZ in Fig. 29(a). As in the $\frac{1}{2}$ CZ statistics in previous figures, the cumulative sample probability shows that roughly 90% of DD is positive. This indicates that an overwhelming portion of prominent returns come from backfacing scarps on B′. (c) The sample probability and (d) cumulative sample probability for DD with respect to the Cory's monostatic source/receiver location over areas where prominent monostatic returns (>60 dB *re*: 1 μPa) are charted for cw transmission s1062 at $2\frac{1}{2}$ CZ in Fig. 29(b). The symmetry of the sample probability in (c) about zero, and the symmetry of the cumulative probability in (d) about 50% are a consequence of the poor resolution of the backscatter charted to B′ for this measurement.

of Naval Research Special Research Program (SRP). The tow-ship track design for the portion of the MAE analyzed in this paper exploits naturally occurring geomorphology to obtain two simultaneous experiments for the price of one. Each experiment measures both long- and short-range bistatic reverberation from one of two bathymetric ridges of distinct geomorphology. We expand upon results obtained at sea[12] and give further evidence that the experiment was highly successful in forecasting prominent reverberation from known bathymetry, and exploiting geomorphology to resolve the ambiguity inherent in horizontal line-array measurements. Specifically, we show that wide-area reverberation in complicated environments such as the western flank of the Mid-Atlantic Ridge can be largely explained with a deterministic model.

For example, we confirm the results of a previous study with lower resolution Acoustic Reconnaissance Cruise (ARC) data[3] by showing that prominent reverberation closely registers with gross ridges, and has a high correlation with negative transmission loss. We also go beyond this previous analysis of ARC data in a number of ways. For example, we use higher resolution MAE waveforms and more sophisticated charting procedures to show that prominent reverberation from a given ridge in the MAR returns primarily from relatively narrow scarps (<1 km) facing the source and receiving arrays.

We show that the deterministic nature of reverberation from a given scarp can be expressed by its stability over differing waterborne measurements. This stability is primarily due to (1) the prominence of such waterborne returns with respect to background levels arising from other sources of reverberation, and (2) the large spatial areas and many

distinct scattering processes averaged over by the towed-array imaging system in a remote survey.

We demonstrate that if the sound-speed structure and bathymetry are well known, right–left ambiguity inherent in the imaging system can be resolved by an environmental symmetry breaking (ESB) technique. This technique requires detailed knowledge of bathymetry and range-dependent propagation modeling to distinguish true from ambiguous returns. While the ESB technique was previously used to resolve gross ridges with ARC data, we show with MAE data that the accuracy of this technique is sufficient to resolve the finer-scale scarps from which prominent reverberation returns. We also demonstrate that right–left ambiguity in the towed-array measurements can be resolved without *a priori* knowledge of bathymetry. We do so with a global inversion (GI) of reverberation charts obtained from differing receiving-array locations and orientations. The GI has not been previously applied to field data and shows close agreement with the ESB method for prominent returns. The GI method also provides sufficient resolution to resolve the finer scale scarps and cliff faces that return prominent reverberation from a given ridge.

The GI has an important practical application. The detailed correspondence found between high-resolution reverberation and geomorphology has significantly strengthened the case for using low-frequency sound as a tool for rapid remote sensing of wide areas of the ocean basin. For this purpose, the propagation modeling used to chart reverberation with known bathymetry in the present analysis could be used to invert for the range and depth of previously uncharted bathymetry. Here, ambiguity in the receiving-array data would have to be resolved by the GI method due to a presumed lack of environmental support for the ESB method. Our results show that the resulting images of bathymetry can be of horizontal resolution approaching that of sidescan sonar intensity measurements over the same area of prominent returns. However, low-frequency towed-array systems can survey hundreds of kilometers within minutes while sidescan sonar systems would take weeks to survey the same area. By analogy, reverberation images are similar in their impact to images produced by medical ultrasound. Just as medical ultrasound is used as a tool to probe inaccessible physiology, towed-array imaging systems can provide a useful tool in identifying the many bathymetric features throughout the worlds oceans that remain uncharted to this day.

Similarly, if the bathymetry is well known, our analysis indicates that measured reverberation can be compared with modeled TL to detect a submerged object by determining whether it is distinguishable from predicted reverberation clutter. Alternatively, such modeling could determine primary locations for a submerged object to hide in reverberation clutter.

Finally, we have found that reverberation from the scarps on a specific lineated ridge (known as B′) vary deterministically as a function of bistatic incident and scattered angle with respect to the ridge axis. For example, we show that the difference between monostatic and bistatic measurements becomes far more pronounced for larger bistatic separations between the source and receiver. In future analysis, we will attempt to parametrize scattering from specific scarps on B′ as a function of bistatic angle. If such a parametrization is stable over distinct scarps on this ridge, it may be of general use for scarps on arbitrary ocean ridges. We will also attempt to more accurately determine the specific geomorphology of the scarps that yield prominent returns. For example, in the present analysis we have shown that prominent returns come from scarps facing the source and receiver, but we have not been able to determine whether steep cliffs (50°–90°) of exposed rock within the scarps are the dominant scatterers or more gradual talus slopes and smaller scale terraces are also important. The fine-scale bathymetry of wavelength-scale resolution collected in support of the MAE should be sufficient to address this last issue, as the preliminary examples in this paper demonstrate. Here, the cross-range orientation of the receiving array will play an important role in making this distinction. For example, when cross range of the receiving array runs skew to the scarp axis, anomalous cliffs within the scarps may be distinguished more accurately. Such analysis may lead to a means of determining the length scales, slope, and orientation of dominant scatterers in a scarp via low-frequency remote sensing.

In conclusion, we observe that it is not cost effective to sample an entire survey area at subwavelength scales to understand wide-area reverberation or scattering. Wide-area measurements inherently average over many scatterers and therefore blur information about individual scattering processes. It is more reasonable to follow the approach of the SRP: (1) Obtain fine-scale environmental information at representative sites; (2) probe these sites with high-resolution measurements at close range to understand the relationship of fine-scale geomorphology and scattering; and (3) use lower resolution measurements at greater ranges to show how individual scattering processes are averaged in wide-area reverberation.

ACKNOWLEDGMENTS

We would like to thank our NRL colleagues Jon Berkson, Matt Healey, George Vermillion, and Richard Wilkerson who were part of our research team during the Main Acoustic Experiment. We also thank the scientists, and crew of the research vessels CORY CHOUEST, ALLIANCE, and KNORR for their efforts in making the Main Acoustics Experiment a success. We thank John Preston (SACLANT) and Brian Gardner (MAI) for many useful discussions about tow-ship track design and logistics before and during the MAE, John Orcutt (SIO), Arthur Baggeroer (MIT), and Bill Hodgkiss (SIO) for many discussions at sea concerning experimental logistics, Kevin Smith (SIO) for at-sea discussions about acoustic propagation, Brian Tucholke (WHOI) for making the SRP Hydrosweep and fine-scale bathymetry available, Ken Stewart (WHOI) for reducing the raw fine-scale data, and the members of the SRP community for many useful discussions and insights. This work was partially supported by the Office of Naval Research. We thank our sponsors Mohsen Badiey and Jeff Simmen for their encouragement.

[1] J. P. Snyder, "Map projections—A working manual," USGS Professional Paper 1395 (1985).
[2] J. Orcutt (Ed.), *Acoustic Reverberation Special Research Program Main Acoustics Experiment, Initial Report* (Scripps Institution of Oceanography, 1993).
[3] N. C. Makris and J. M. Berkson, "Long-range backscatter from the Mid-Atlantic Ridge," J. Acoust. Soc. Am. **95**, 1865–1881 (1994).
[4] N. C. Makris, R. Menis, and L. Z. Avelino (unpublished).
[5] N. C. Makris, "Imaging ocean-basin reverberation via inversion," J. Acoust. Soc. Am. **94**, 983–993 (1993).
[6] J. R. Preston, T. K. Akal, and J. M. Berkson, "Analysis of backscattering data in the Tyrrhenian Sea," J. Acoust. Soc. Am. **87**, 119–134 (1990).
[7] B. E. Tucholke and J. Lin, "A geological model for the structure of ridge segments in slow spreading ocean crust," J. Geophys. Res. **99**, 11,937–11,958 (1994).
[8] N. C. Makris, "Proposed experiment," in Acoustic Reverberation Special Research Program Research Symposium, Woods Hole Oceanographic Institution (1992).
[9] M. D. Collins, "A self-starter for the parabolic equation method," J. Acoust. Soc. Am. **92**, 2069–2074 (1992).
[10] N. C. Makris and B. Gardner, "Planned tracks/waypoints, runs 3–9," in Acoustic Reverberation Special Research Program Main Acoustics Experiment, Initial Report, Scripps Institution of Oceanography (1993), pp. 65–80. [J. R. Preston proposed and gave the initial design for the "Diffraction Experiment" portion of run 6 (ALLIANCE crossover B′), and suggested the ALLIANCE tracks for run 9 (during which time the CORY crossed over C′).]
[11] SRP 15-kHz Hydrosweep bathymetry data were acquired in August 1992 during the SRP Geophysical Survey. The Principal Investigator B. E. Tucholke, and Co-Principal Investigators M. C. Kleinrock and J. Lin are from the Woods Hole Oceanographic Institution.
[12] N. C. Makris, L. Avelino, R. Menis, and J. M. Berkson, "Preliminary results: Correlation between reverberation and geomorphology," in Acoustic Reverberation Special Research Program Main Acoustics Experiment, Initial Report, Scripps Institution of Oceanography (1993), pp. 336–355.
[13] W. S. Hodgkiss, J. C. Nickles, G. L. Edmonds, R. A. Harris, and G. L. D'Spain, "A large dynamic range vertical array of acoustic sensors," in *Full Field Inversion Methods in Ocean and Seismic Acoustics*, edited by O. Diatchok, A. Ciaiti, P. Gerstoff, and H. Schmidt (Kluwer, Dordrecht, 1994).
[14] C. C. Goad, convenor, "Positioning with GPS-1985," in *Proceedings First International Symposium on Precise Positioning with the Global Positioning System* (National Geodetic Information Center, NOAA, Rockville, Maryland, 1985), Vol. 1.
[15] G. I. Evenden, "Cartographic projection procedures for the Unix environment—a user's manual," USGS Open-File Rep. 90-284, 1991.
[16] J. W. Goodman, *Statistical Optics* (Wiley, New York, 1985).
[17] S. O. Rice, "Mathematical analysis of random noise," Bell Syst. Tech. J. **24**, 46–108 (1945).
[18] I. Dyer, "Statistics of sound propagation in the ocean," J. Acoust. Soc. Am. **48**, 337–345 (1970).
[19] N. C. Makris, "A parameter estimation bound for images," submitted to J. Acoust. Soc. Am.
[20] N. C. Makris, "MFA beampattern," in Acoustic Reverberation Special Research Program Main Acoustics Experiment, Initial Report, Scripps Institution of Oceanography (1993), pp. 204–208.
[21] A. B. Baggeroer, "Transmission nomenclature," in Acoustic Reverberation Special Research Program Main Acoustics Experiment, Initial Report, Scripps Institution of Oceanography (1993), pp. 135–153.
[22] B. D. Steinberg, *Principles of Aperture and Array Design* (Wiley, New York, 1976).
[23] SRP 120-kHz DSL 120 bathymetry data were acquired in May–June of 1993 during the SRP Fine-Scale Geophysical Survey with Principal Investigator B. E. Tucholke. Ken Stewart was responsible for conversion of raw data to the 5-m gridded bathymetry. Both investigators are from the Woods Hole Oceanographic Institution.
[24] B. E. Tucholke, Woods Hole Oceanographic Institution (personal communication).
[25] J. R. Preston, E. Michelozzi, L. Troiano, and R. Hollet, "Cruise report on RV ALLIANCE cruise MARE July 5–August 1, 1993 SACLANTCEN's joint experiment with ONR's ARSRP Group," SACLANT Undersea Research Centre, LaSpezia, Italy (1993).
[26] J. R. Preston and W. A. Kinney, "Monostatic and bistatic reverberation results using linear frequency modulated pulses," J. Acoust. Soc. Am. **93**, 2549–2565 (1993).